Geoscientific
Model Development

pyVPRM: a next-generation vegetation photosynthesis and respiration model for the post-MODIS era

Theo Glauch[1,2], **Julia Marshall**[1], **Christoph Gerbig**[3], **Santiago Botía**[3], **Michał Gałkowski**[3,4], **Sanam N. Vardag**[2,5], **and André Butz**[2,5]

[1]Deutsches Zentrum für Luft- und Raumfahrt, Institut für Physik der Atmosphäre, Oberpfaffenhofen, Germany
[2]Institute of Environmental Physics, Heidelberg University, Heidelberg, Germany
[3]Max Planck Institute for Biogeochemistry, Jena, Germany
[4]Faculty of Physics and Applied Computer Science, AGH University of Kraków, Kraków, Poland
[5]Heidelberg Center for the Environment, Heidelberg University, Heidelberg, Germany

Correspondence: Theo Glauch (theo.glauch@dlr.de)

Abstract. The Vegetation Photosynthesis and Respiration Model (VPRM) is a well-established tool for estimating carbon exchange fluxes between the atmosphere and the biosphere. The gross primary production (GPP) and respiration (R_{eco}) of the ecosystem are modeled separately at high spatial and temporal resolution using the satellite-derived enhanced vegetation index (EVI) and land surface water index (LSWI), as well as meteorological variables for solar irradiance and surface temperature. The net ecosystem exchange (NEE) is calculated as the difference between the gross flux GPP and respiration. VPRM is widely used as a biospheric flux model in atmospheric transport modeling, most often on scales ranging from city to continent, but also in studies of biospheric carbon budgets and their changes with climate extremes. Historically, satellite-based surface reflectances from the 500 m resolution Moderate Resolution Imaging Spectroradiometer (MODIS) have been used to determine the EVI and LSWI. However, MODIS is reaching the end of its lifetime and will soon be decommissioned. Therefore, we present an updated version of VPRM, *pyVPRM*, which provides a software framework with a modular structure that can be used with various satellite products, land cover maps, meteorological data sources, and VPRM model parameterizations. Our tool naturally provides an interface to use satellite data from Sentinel-2, MODIS, and VIIRS, as well as global high-resolution land cover classification maps from the Copernicus Dynamic Land Cover Collection 3 and ESA WorldCover at 100 and 10 m resolution, respectively.

Neither product is static; hence, dynamic changes of the land cover from year to year can be represented. Using Sentinel-2, ecosystem fluxes can be calculated at a resolution of up to 20 m, providing more accurate flux estimates in heterogeneous landscapes like croplands and making it possible to resolve small-scale vegetation patches common in urban areas. In contrast, VIIRS data are at the same resolution as MODIS and thus can provide continuity once MODIS is discontinued, requiring only minor adjustments to the VPRM data preprocessing. In addition, *pyVPRM* improves the data handling, for example, for snow-covered scenes. This paper presents the *pyVPRM* framework, discusses changes and improvements compared to previous VPRM implementations, and provides VPRM parameters for the European domain based on indices calculated from MODIS, Sentinel-2, and VIIRS using a new selection of eddy-covariance observations from 97 flux tower sites. Using *pyVPRM* and the new parameters, we observe significant improvements in the estimation of the European carbon budget. The results conform well with those from inversion studies.

1 Introduction

Carbon dioxide (CO_2) is the most important anthropogenically influenced greenhouse gas in the Earth's atmosphere and plays a decisive role in the carbon cycle. Carbon cycling occurs between the different compartments/reservoirs

(i.e., atmosphere, oceans, and biosphere) of the Earth system on different timescales. The largest exchange flux of carbon is between the atmosphere and the terrestrial biosphere (Friedlingstein et al., 2023). This uptake flux is driven by the biosphere's photosynthesis (gross primary production, or GPP), i.e., the conversion of carbon dioxide, light, and water into sugar and oxygen. At the same time, carbon dioxide is released back to the atmosphere by respiration from plants and soil. The net vegetation flux into the atmosphere, i.e., the net ecosystem exchange (NEE), is given by the difference between the GPP and respiration. With a yearly global GPP of around 120 GtC, biospheric carbon dioxide fluxes are about an order of magnitude larger than anthropogenic emissions (with a yearly emission of 11.1 GtC in 2022; see Friedlingstein et al., 2023). Clearly, biospheric fluxes have an important impact on the time-dependent CO_2 concentrations in the atmosphere. Over longer timescales, GPP and respiration are nearly in balance, with a net carbon sink of around 3 GtC per year (Friedlingstein et al., 2023).

Terrestrial biosphere models (TBMs) are commonly used to simulate the carbon exchange between the biosphere and the atmosphere. They can be used to study the carbon budget of the terrestrial biosphere, as well as the impact of droughts and other climate extremes (Thompson et al., 2020; Stocker et al., 2019). Frequently, TBM outputs are also used as an input in atmospheric transport models, e.g., for the (inverse or top-down) estimation of carbon budgets from anthropogenic and natural sources from city to global scales (Bousquet et al., 1999; Sargent et al., 2018). Those top-down estimates of anthropogenic CO_2 emissions, informed by atmospheric concentration measurements, are expected to become an integral part of the global stocktakes required by international climate treaties (Maksyutov et al., 2019). They provide complementary information to the "bottom-up" methods, which combine activity data with emission factors to derive the budget (Choulga et al., 2021).

There are several TBMs that utilize remote-sensing data to locally estimate the plant and water dynamics (Nelson et al., 2024; Gerbig and Koch, 2021; Randerson et al., 1996; Running and Zhao, 2021). The Vegetation Photosynthesis and Respiration Model (VPRM) is a well-established light-use-efficiency TBM that estimates GPP, respiration, and, consequently, NEE from satellite-derived indices and meteorological drivers (Mahadevan et al., 2008). VPRM parameters are estimated using in situ measurements from eddy-covariance flux towers in different regions, for different years, and across different vegetation classes. Historically, VPRM has mainly been used with observations from the 500 m resolution Moderate Resolution Imaging Spectroradiometer (MODIS) instrument, installed on board the Terra and Aqua satellites[1],

combined with the 1 km resolution SYNMAP land cover classification map (Jung et al., 2006).

Several modifications of the standard VPRM have been discussed in the literature. A common modification is a more sophisticated term for R_{eco} by, for example, including additional information on water stress (Gourdji et al., 2022) or adjusting the temperature response function (Sun et al., 2023). Other customized VPRM applications are the Urban-VPRM model for cities (Hardiman et al., 2017), the Polar-VPRM for high-latitude ecosystems (Luus and Lin, 2015), a regional version for China (China-VPRM, Dayalu et al., 2018), approaches that incorporate information from solar-induced fluorescence (Commane et al., 2017), and a version to run online in the greenhouse gas module of the Weather Research and Forecasting (WRF) model (Ahmadov et al., 2009). All of these VPRM implementations rely on indices derived from MODIS.

The first MODIS sensor was launched in 1999, and since then the series of instruments have provided nearly a quarter-century time series of consistent data with high temporal resolution. Due to an onboard fuel shortage, MODIS will be decommissioned at the end of 2025, and hence alternative data sources are needed for VPRM.

In this paper, we present a new software package – *pyVPRM* (https://github.com/tglauch/pyVPRM, last access: 24 July 2025) – which adapts the VPRM to the post-MODIS era. It has an interface for new satellite datasets (Sentinel-2, VIIRS) and high-resolution land cover products (Copernicus Dynamic Land Cover Collection 3, Buchhorn et al., 2020; ESA WorldCover, Zanaga et al., 2022; and MapBiomas, Souza et al., 2020). Furthermore, it provides several improvements in terms of data handling, including the treatment of snow-covered scenes to improve stability and the use of the actual observation time when using time-aggregated products (like the 8 d MODIS products MOD09A1 (Vermote, 2021a) and MYD09A1 (Vermote, 2021b)) in the data smoothing process. In summary, those changes allow for a more accurate estimation of biospheric carbon dioxide fluxes, especially in regions with highly heterogeneous landscapes like cities or croplands. Thanks to its modular structure, *pyVPRM* can be easily extended by users to include further satellite products, land cover maps, meteorological datasets, and VPRM implementations.

This paper is structured as follows: in Sect. 2, we review the methodology of the standard VPRM model (Mahadevan et al., 2008). In Sect. 3, we discuss the improvements and changes in *pyVPRM*. In Sect. 4, we describe the estimation of the VPRM parameters for MODIS, VIIRS, and Sentinel-2 using a new selection of European flux tower sites. In Sect. 5, we discuss those parameters and their implications for European biospheric fluxes. In Sect. 6, we provide a discussion on the improvements, and we conclude in Sect. 7 with a summary and an outlook. A brief overview of the code structure is provided in Appendix A.

---

[1]MODIS bands 1 and 2 have a 250 m resolution. Throughout this paper, we define the VPRM model resolution as the lowest resolution among all the required bands.

2 Review of the VPRM model

It should be noted that VPRM is not a centrally managed model, and implementations present throughout the literature differ significantly in their choices of vegetation classes and model equations. In this paper, we focus only on the original VPRM model implementation (Mahadevan et al., 2008) (called the *vprm_base* module in *pyVPRM*). For Mahadevan et al. (2008), eight vegetation classes are used: evergreen forest, deciduous forest, mixed forest, shrubland, savanna, cropland, grassland, and urban/non-vegetated.

All VPRM model implementations split the CO_2 flux between the terrestrial biosphere and atmosphere into two parts: gross primary production (GPP), driven by photosynthesis, and the sum of soil and plant respiration. In the standard VPRM (Mahadevan et al., 2008), the GPP is parameterized as

$$\text{GPP} = \epsilon \times \frac{1}{1 + \text{PAR}/\text{PAR}_0} \times \text{PAR} \times \text{EVI}. \tag{1}$$

Here, EVI is the remote-sensing-based enhanced vegetation index (EVI), which is closely related to the productivity of vegetation (Huete et al., 2002). It is used as a measure of the fraction of absorbed photosynthetically active radiation (fAPAR, at wavelengths between around 400 and 700 nm) available for photosynthesis. EVI is usually based on measurements in the red, near-infrared, and blue bands, but a variant of this index can be calculated using only the red and infrared bands (see Sect. 3.1.1 for details). In contrast to other vegetation indices, like the normalized difference vegetation index (NDVI, Rouse et al., 1974), EVI is more sensitive to variations in canopy structure, including leaf area index (LAI), canopy type, and plant physiognomy (Huete et al., 2002).

The total amount of incoming photosynthetically active radiation can be approximated through the incoming shortwave (SW) radiation (direct and diffuse) at the surface using the relationship $\text{PAR} \approx \text{SW}/0.505$ (Mahadevan et al., 2008). The term $1/(1 + \text{PAR}/\text{PAR}_0)$ describes the saturation of the plants' photosynthetic activity. PAR_0 is the half-saturation value, one of the parameters fitted in the model for each vegetation class. Finally, ϵ is the light-use efficiency, which is the product of four terms with values between 0 and 1:

$$\epsilon = \lambda \times T_{\text{scale}} \times W_{\text{scale}} \times P_{\text{scale}}. \tag{2}$$

Here, T_{scale} describes the temperature dependence of the photosynthesis, defined as

$$T_{\text{scale}} = \frac{(T - T_{\text{min}})(T - T_{\text{max}})}{(T - T_{\text{min}})(T - T_{\text{max}}) - (T - T_{\text{opt}})^2}, \tag{3}$$

with T_{min}, T_{opt}, and T_{max} referring to literature-derived values of the minimal, optimal, and maximal temperatures for photosynthesis for each vegetation class in degrees Celsius. At temperatures below T_{min} or above T_{max}, photosynthetic activity is set to 0. Usually, the temperature T is given by the 2 m temperature, which is available in most meteorological models.

The variable P_{scale} accounts for the effect of leaf age and is defined separately for the different vegetation types. For evergreen forests,

$$P_{\text{scale}} = 1; \tag{4}$$

for grassland and savannas,

$$P_{\text{scale}} = (1 + \text{LSWI})/2; \tag{5}$$

and for all other vegetation classes,

$$P_{\text{scale}} = \begin{cases} 1, & \text{between leaf full expansion and senescence (EVI > TH}_{\text{leaf full expansion}}) \\ (1 + \text{LSWI})/2, & \text{during bud burst to leaf full expansion and during senescence (EVI} \leq \text{TH}_{\text{leaf full expansion}}) \end{cases}. \tag{6}$$

Here, LSWI is the land surface water index, which captures the effects of water stress and leaf phenology and is derived using satellite data in the near and shortwave infrared (see Sect. 3.1.1 for details). The periods from bud burst to leaf full expansion and senescence are defined as those where the EVI is below a threshold of

$$\text{TH}_{\text{leaf full expansion}} = \text{EVI}_{\text{min}} + 0.55 \cdot (\text{EVI}_{\text{max}} - \text{EVI}_{\text{min}}). \tag{7}$$

Both the maximum and minimum EVI values (EVI_{max} and EVI_{min}) are calculated for each satellite pixel over an entire year.

The variable W_{scale} represents the canopy water content as a measure of the water stress. It is defined as

$$W_{\text{scale}} = \begin{cases} \frac{\text{LSWI} - \text{LSWI}_{\text{min}}}{\text{LSWI}_{\text{max}} - \text{LSWI}_{\text{min}}}, & \text{grassland and savanna}, \\ \frac{1 + \text{LSWI}}{1 + \text{LSWI}_{\text{max}}}, & \text{all other classes}. \end{cases} \tag{8}$$

The LSWI thresholds, LSWI_{max} and LSWI_{min}, are calculated as the pixel-wise maximum/minimum LSWI during the growing season (Eq. 7). Using this threshold ensures that the maximum LSWI lies within the growing season. This is important because LSWI is sensitive to snow periods.

Note that for grassland, we follow the parameterization of Matross et al. (2006), which takes into account that grasslands are xeric ecosystems. This represents a deviation from the work of Mahadevan et al. (2008) relevant for Eqs. (5) and (8).

Finally, λ is a fitting parameter that accounts for the quantum yield and also includes vegetation-class-specific (linear) corrections to the other parameters. For well-watered C_3 plants, the quantum yield is expected to be around 1/6 (Mahadevan et al., 2008).

The parameterization of ecosystem respiration, R_{eco}, is a simple linear function with two free parameters, α and β:

$$R_{\text{eco}} = \alpha \times \max(T, T_{\text{low}}) + \beta. \tag{9}$$

When $T < T_{\text{low}}$, the temperature in Eq. (9) is set to T_{low} to maintain a minimal level of respiration, as the (winter) soil temperature is typically higher than the air temperature.

In summary, four free parameters α, β, PAR_0, and λ have to be fitted for each vegetation type.

3 The *pyVPRM* package

With *pyVPRM*, we provide a Python-based software package that can be used for a wide range of applications of the Vegetation Photosynthesis and Respiration Model (VPRM). It has a modular structure and can be used to combine different satellite data products, land cover maps, meteorology datasets, and VPRM model parameterizations. It provides all functions to fit VPRM parameters, produce biospheric fluxes, and generate input files for using VPRM online in mesoscale atmospheric transport models like the Weather Research and Forecasting model (WRF-GHG, Beck et al., 2012/WRF-Chem, Peckham, 2012) or the ICON-ART model (Schröter et al., 2018). An overview of the modular structure of *pyVPRM* is given in Fig. 1.

3.1 Satellite data

In general, all multi-spectral satellites that have at least a near-infrared, a short wavelength infrared, and a red channel are suitable for constructing the indices required in the VPRM model. In addition, a blue band can be useful for the calculation of the enhanced vegetation index (EVI) but is not strictly necessary. While MODIS has been used historically, other satellite datasets are now available as well. Notably, Sentinel-2 (ESA, 2022) improves the VPRM spatial resolution from 500 m (MODIS (Vermote, 2021a, b; Vermote and Wolfe, 2021, ?), VIIRS (Vermote et al., 2023a, b)) down to 20 m, which is especially useful for modeling ecosystem carbon dioxide fluxes in urban areas or in heterogeneous landscapes such as croplands and agricultural grasslands. The choice of satellite mission ultimately depends on the specific user requirements, e.g., the required spatial resolution, data availability, and satellite revisit time, especially when persistent cloud cover is an issue.

In its current implementation, *pyVPRM* provides an interface for satellite data products from MODIS, VIIRS, and Sentinel-2. Due to the modular structure, *pyVPRM* can be extended to other missions (e.g., Landsat) or fusion products of different satellite missions (e.g., Moreno-Martínez et al., 2020). VIIRS is of particular interest, as it is the drop-in replacement for MODIS after its discontinuation. A summary of the three satellite missions and the relevant mission specifications are given in Table 1. Evidently, there is a large overlap between the wavelength bands among the missions. Nevertheless, we fit a different set of VPRM parameters for each mission, accounting also for differences in the data processing, like the atmospheric correction.

The MODIS sensor is placed on two research satellites – Aqua and Terra – with afternoon and morning orbits, respectively. Hence, combining data from the two satellite missions helps to mitigate sparse observations and improve the modeling of vegetation dynamics. This is especially useful in regions with high cloud coverage like the tropics. MODIS (Terra, Aqua) and VIIRS products are available as daily observations (MOD09GA, MYD09GA, VNP09GA) and as aggregated 8 d products (MOD09A1, MYD09A1, VNP09H1). The choice of optimal product depends on the expected vegetation dynamics and available computing resources. In this work, we use daily MODIS and VIIRS data, i.e., MOD09GA, MYD09GA, and VNP09GA.

3.1.1 Satellite indices

EVI is sensitive to the leaf area index, canopy type, and plant physiognomy. It is defined using the reflectances in red (ρ_{Red}), infrared (ρ_{NIR}), and blue (ρ_{Blue}) following Huete et al. (2002) as

$$\text{EVI} = G \times \frac{(\rho_{\text{NIR}} - \rho_{\text{Red}})}{(\rho_{\text{NIR}} + C_1 \times \rho_{\text{Red}} - C_2 \times \rho_{\text{Blue}} + L)}, \quad (10)$$

where, in general, the free parameters G, C_1, C_2, and L depend on the satellite sensor. In our case, we use $G = 2.5$, $C_1 = 6$, $C_2 = 7.5$, and $L = 1$ (Huete et al., 2002) for both MODIS and Sentinel-2. While the detection of vegetation is governed by the red and infrared bands, the blue channel was added to account for the impact of atmospheric aerosols. It is, however, also possible to define an alternate enhanced vegetation index without a blue band (Jiang et al., 2008), EVI2, as

$$\text{EVI2} = G \times \frac{(\rho_{\text{NIR}} - \rho_{\text{Red}})}{(\rho_{\text{NIR}} + C_1 \times \rho_{\text{Red}} + L)}, \quad (11)$$

with only three free parameters, i.e., G, C_1, and L. In our case, we use EVI2 for data from the VIIRS satellite, as no blue band is available. Here, the free parameters are set to $G = 2.5$, $C_1 = 2.4$, and $L = 1$ (Huete et al., 2002).

In addition to EVI, VPRM uses another remote-sensing-based index – the land surface water index (LSWI) – to estimate the vegetation and soil water content. LSWI requires a near-infrared and a shortwave infrared band and is calculated for all satellite missions following Gao (1995) as

$$\text{LSWI} = \frac{\rho_{\text{NIR}} - \rho_{\text{SWIR}}}{\rho_{\text{NIR}} + \rho_{\text{SWIR}}}. \quad (12)$$

In *pyVPRM*, both EVI and LSWI are calculated within the VPRM preprocessor class (see Fig. 1) whenever a new satellite image is added to the instance (using the *add_sat_img(.)* function). The implementation of *pyVPRM* allows the user to adjust the free parameters in the function call or even add an entirely different implementation of satellite indices.

3.1.2 Data quality masking

Not every satellite observation is useful for the estimation of EVI and LSWI. Typical problems include cloudiness, shadows, and problems in the satellite retrieval. In order to get a reliable estimate of the time evolution of the two indices, pixels that have any of the previously mentioned problems are
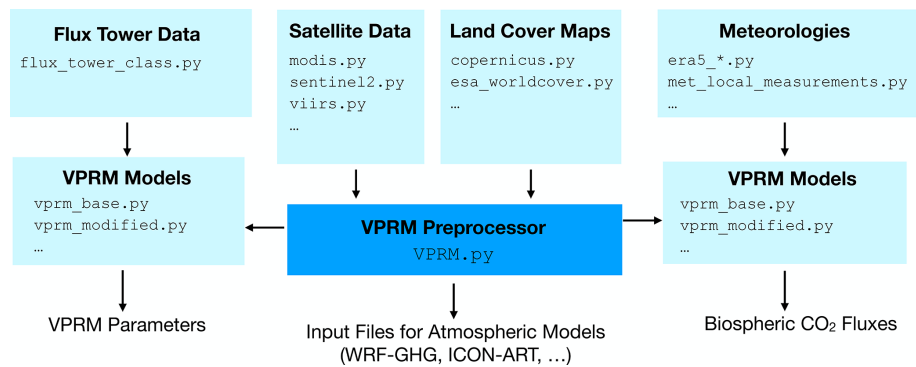
Figure 1. Modular structure of *pyVPRM*. Using different combinations of inputs, one can either calculate VPRM parameters, generate VPRM input files for atmospheric models, or calculate "offline" biospheric carbon dioxide fluxes. The type of module is shown in bold with the corresponding (exemplary) file name below. This is subject to changes and extensions in the further development of the model. The VPRM preprocessor is the central class that prepares the satellite images and land cover maps, as described in Sect. 3.1–3.3. More details are found in Appendix A.

Table 1. Overview of the relevant properties of the different satellite missions. The spatial resolution is given as the minimal resolution of all bands required for the VPRM calculations. In addition, the table names the MODIS (Vermote and Wolfe, 2021, ?; Vermote, 2021a, b), VIIRS (Vermote et al., 2023a, b), and Sentinel-2 (ESA, 2022) data products used for the VPRM calculations in this paper. Note that for Sentinel-2, there is a slight difference in the bands between Sentinel-2A and Sentinel-2B. The values given here represent the bands of Sentinel-2A.

Feature	MODIS (Terra, Aqua)	VIIRS (Suomi NPP)	Sentinel-2A and 2B
Red band [nm]	620–670 (Band 1)	600–680 (Band I1)	664.6 ± 31 (Band 4)
Near-infrared band (NIR) [nm]	841–876 (Band 2)	846–885 (Band I2)	864.7 ± 21 (Band 8A)
Shortwave infrared band (SWIR) [nm]	1628–1652 (Band 6)	1580–1640 (Band I3)	1613.7 ± 91 (Band 11)
Blue band [nm]	459–479 (Band 3)	–	492.4 ± 66 (Band 2)
Spatial resolution	500 m	500 m	20 m
Revisit frequency (at Equator)	1–2 d	1–2 d	5 d
Data availability	1999–now	2011–now	2015–now
Data products	MOD09GA, MYD09GA MOD09A1, MYD09A1	VNP09GA VNP09H1	Sentinel-2 Collection 1 Level-2A

masked out from all further calculations using the data quality flags of the respective data products. Specifically, we use only pixels that have the highest-quality data in all bands, do not show any kind of cloud cover (also cirrus), and are free from cloud shadows. Periods with snow are treated differently; see Sect. 3.1.3. Details on the data quality flags for the satellite products discussed in this paper can be found in Table B1 (for MODIS), Table B2 (for VIIRS), and Table B3 (for Sentinel-2). In *pyVPRM*, the *mask_bad_pixels(.)*, *mask_bad_clouds(.)*, and *mask_bad_snow(.)* functions of the respective satellite image class are used.

3.1.3 Time smoothing

We expect both LSWI and EVI to be continuous functions over the year. Hence, in order to remove statistical noise, we derive daily indices through a temporal smoothing pro-

cedure (Mahadevan et al., 2008). In the first step, all the available satellite scenes for at least a year are loaded and combined into a data cube with two spatial dimensions and a time dimension. Subsequently, the array of observations in each pixel is smoothed using a *lowess* (LOcally WEighted Scatterplot Smoothing) function (Cleveland, 1979) (using the *lowess(.)* function of the VPRM preprocessor). The smoothing takes into account the specific observation time of each scene, even if 8 d products (like MOD09A1) are being used. Finally, the fitted lowess function is evaluated for each day of the year, producing a data cube storing daily EVI and LSWI for each pixel. It is good practice to include additional satellite scenes before the beginning and after the end of the year of interest to avoid boundary effects.

While the lowess function is fairly stable against noise, instabilities may arise if the vegetation is covered by snow
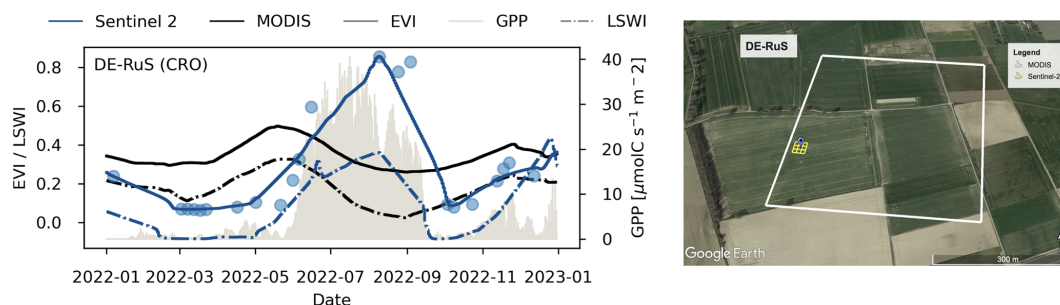
Figure 2. Left panel: comparison of the hourly GPP at the cropland flux tower site Selhausen Juelich (DE-RuS; 50.8659° N, 6.4471° E) with the satellite indices (EVI, LSWI) for Sentinel-2 and MODIS over the year 2022. GPP (in light gray) is based on the ICOS daytime partitioning method. The solid and dash-dotted lines show the lowess-smoothed LSWI and EVI, respectively. Values from MODIS are shown in black, while values for Sentinel-2 are shown in blue. The blue points show the unfiltered EVI measurements for the case of Sentinel-2. Right panel: satellite image of the site with the relevant MODIS (white) and Sentinel-2 (yellow) pixels overlaid. The position of the flux tower is shown with a blue pin. Map data © Google Earth 2024.

for several months of the year (especially at high latitudes). Hence, instead of masking out every observation with detected snow cover, as we do for clouds and other low-quality observations, during snow-covered periods, we set the EVI and LSWI to the minimum value observed outside of the snow-covered period. This stabilizes the numerical fit and does not impact the estimated carbon fluxes, as the temperature during snow-covered periods is usually below 0° C, resulting in negligible GPP (see Eq. 3). The respiration, on the other hand, is independent of the satellite indices.

Figure 2 shows an example of the lowess-filtered values for EVI and LSWI from MODIS and Sentinel-2 at the German cropland flux tower site Selhausen Juelich (DE-RuS; 50.8659° N, 6.4471° E) in 2022. For comparison, hourly measured GPP is shown in the background. On average, the crosswind integrated distance, which contributes 90% of the flux measurement, is around 85 m at the eddy-covariance site DE-RuS (ICOS RI et al., 2023). A 2D map of the footprint is shown in Fig. 2b of Paulus et al. (2024). Evidently, the disagreement of the MODIS EVI curve with the measured GPP is a direct result of the limited spatial resolution of MODIS in such a heterogeneous landscape. In fact, the observed seasonal cycle of the satellite indices is a superposition of the seasonal cycles of the fields contained within the MODIS pixel (white). The field containing the flux tower itself was growing potatoes in 2022, which are only planted in April, take time to grow, and last until fall. The eastern and southeastern neighboring fields, in contrast, had winter wheat, which was sown the fall before, starts photosynthesis early, and is typically harvested around July (Marius Schmidt, personal communication, 2025). In contrast, the Sentinel-2 indices more closely follow the seasonal cycle of the GPP measurements. Uncertainties in Sentinel-2 arise mainly through the limited revisit frequency. While MODIS provides one image every 1–2 d under clear-sky conditions, Sentinel-2 takes only one image every ~ 5 d. Hence, in time periods with frequent cloud coverage, observations can become sparse. The resulting interpolation errors are largest in periods of strong leaf phenological change.

We have exemplarily studied the impact of the revisit time for three flux tower sites with very homogeneous landscapes on the spatial scale of a MODIS pixel; see Fig. 3. For MODIS, we have used the daily Terra and Aqua observations (MOD09GA, Vermote and Wolfe, 2021/MYD09GA, Vermote, 2021a), and for Sentinel-2, Collection 1 Level-2A data from Sentinel-2A and 2B (ESA, 2022). The EVI curves for both satellites show a similar behavior. Small differences between the absolute EVI values are expected due to differences in the observation channels and resolutions. While Sentinel-2 curves show a little bit more instability, this is a minor effect on absolute scales. In general, we expect the instability of the smoothing to increase for regions with very frequent cloud coverage or long times without daylight (as in northern Scandinavia).

3.2 Land cover classification

The standard VPRM model (Mahadevan et al., 2008), as described in Sect. 2, is fitted with four independent parameters for each vegetation class. In addition to remote sensing data, the estimation of terrestrial carbon fluxes with VPRM therefore requires a land cover classification map that covers the entire area of interest. In general, *pyVPRM* can be used with any kind of land cover product and vegetation classification. By default, the package provides interfaces for the global 100 m Copernicus Dynamic Land Cover Collection 3 (Buchhorn et al., 2020) and the global 10 m ESA WorldCover (Zanaga et al., 2022) product. Neither product is static in that they provide different maps for different years to account for land use changes.

In addition, both land cover products do not provide a dedicated savanna class. We therefore drop it, which is reasonable for most parts of the mid-latitudes. In regions where this vegetation class is needed, it is advisable to use a dedicated
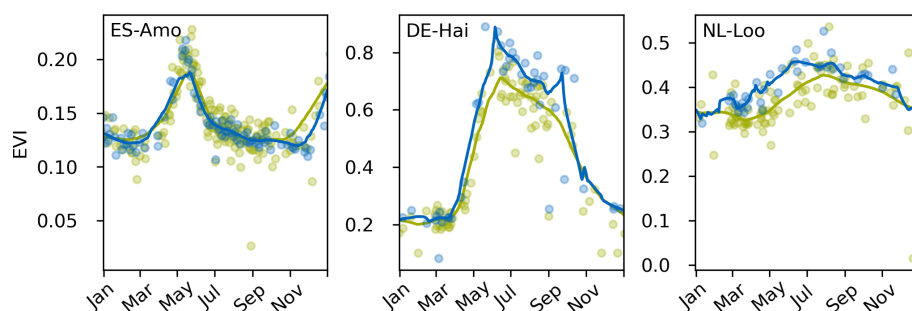
Figure 3. Development of the EVI for three test sites with different vegetation types in 2022: ES-Amo (shrubland), DE-Hai (deciduous forest), and NL-Loo (evergreen forest). Blue and green lines show the lowess-smoothed curves for Sentinel-2 and MODIS, respectively. The dots in the background show the cloud- and snow-filtered satellite observations.
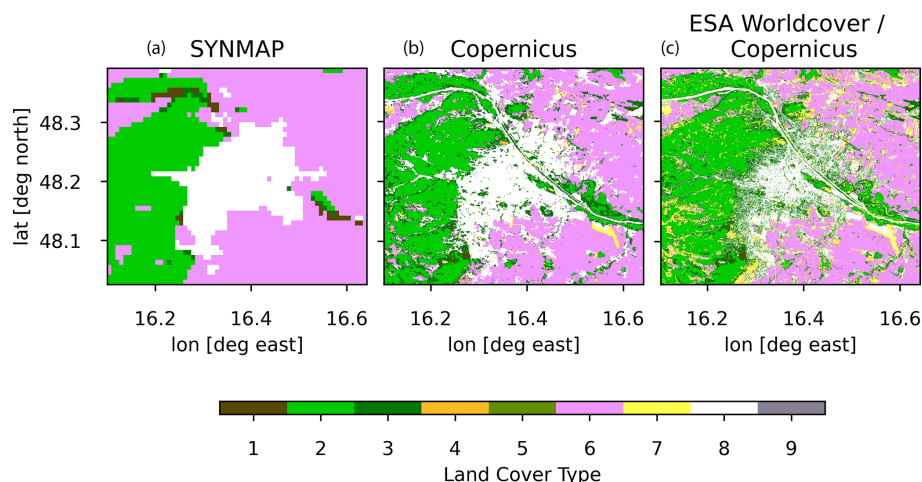

Figure 4. The region around Vienna for three different land cover classification products: SYNMAP **(a)**, the 100 m product of the Copernicus Dynamic Land Cover Collection 3 **(b)**, and a hybrid between ESA WorldCover and the Copernicus Dynamic Land Cover Collection 3 **(c)**. Different colors (numbers) represent the different vegetation classes in our VPRM model for Europe: evergreen (1), deciduous forest (2), mixed forest (3), shrubland (4), cropland (6), grassland (7), non-vegetated area (8), and wetland (9). The class savanna (5) is not used in this implementation but remains in the numbered list for legacy reasons.

land cover product and VPRM parameters. On the contrary, we have decided to add a new class for wetland. This is motivated by the larger amount of available flux tower measurements (cf. Fig. 6).

Table 2 shows the mapping between the land cover types for the two products and the eight VPRM classes used in this paper. Note that ESA WorldCover has only one forest class and, therefore, contains no information on the forest type. Hence, it is rational to generate a hybrid product that uses ESA WorldCover as a baseline but replaces the forest subclass information with that of the (lower-resolution) Copernicus Dynamic Land Cover Collection 3 (Buchhorn et al., 2020). A sequence of land cover maps with increasing resolution is shown for a region around Vienna in Fig. 4. Note that while SYNMAP (Jung et al., 2006) does not resolve much of the structure inside the built-up urban area, the Copernicus Dynamic Land Cover Collection 3 (Buchhorn et al., 2020) product and especially the hybrid product can resolve vege-

tated areas within the built-up area and heterogeneity within the forested area to the west of the city and the surrounding croplands.

In many cases, the land cover maps will not have the same coordinate reference system and resolution as the satellite data products. Hence, the land cover map needs to be regridded to match the satellite data. *pyVPRM* uses the xESMF package (Zhuang et al., 2023), which is based on the Earth System Modeling Framework (ESMF) (Hill et al., 2004). xESMF supports general curvilinear grids and different regridding algorithms, most importantly bilinear and conservative, in order to preserve total quantities. Using conservative regridding, the *add_land_cover_map(.)* function of *pyVPRM*'s VPRM preprocessor calculates the fraction of each land cover class from the input (land cover) grid for each pixel in the destination (satellite) grid. The result is a 2D vegetation fraction map for each vegetation class with

Table 2. Mapping from land cover classifications in the Copernicus Dynamic Land Cover Collection 3 (Buchhorn et al., 2020) and ESA WorldCover (Zanaga et al., 2022) to the eight VPRM classes used in this paper. The numbers represent the internal land cover codes of the two data products. Note (*) that ESA WorldCover has only one forest class. Hence, it is advised to use a hybrid of the two products in this table, using the forest-type classification of the 100 m products of the Copernicus Dynamic Land Cover Collection 3. *pyVPRM* uses YAML configuration files to define the mapping and auxiliary data for the vegetation classes.

	Copernicus Dynamic Land Cover Collection 3	ESA WorldCover
Evergreen forest	111, 112, 121, 122	10*
Deciduous forest	113, 114, 123, 124	10*
Mixed forest	115, 126, 116, 125	10*
Shrubland	20	20
Cropland	40	40
Grassland	30, 100	30, 100
Non-vegetated	50, 60, 70, 80, 200	50, 60, 70, 80
Wetland	90	90, 95

the same spatial extent and on the same grid as the satellite scenes.

3.3 VPRM data preparation and calculation of carbon fluxes

In order to generate the VPRM fluxes for a given region, we use Eqs. (1) and (9) in matrix form. This requires the meteorological data (e.g., temperature and solar irradiance) and the land cover information to be regridded onto the native satellite grid using the *xESMF* package; see Sect. 3.2. With all the data on the same grid, the net ecosystem exchange (or GPP and respiration) for each land cover type is calculated by matrix multiplication (using the *make_vprm_predictions(.)* function of the VPRM model class). Summing up all land cover types with their respective fractional weight, F_v, gives the total flux per pixel, i.e.,

$$
\begin{aligned}
\text{NEE}_{2D} = \sum_{\substack{v \in \\ \text{veg classes}}} F_v &\times \big[-\big(\lambda_v \times T_{\text{scale},v} \times W_{\text{scale}} \times P_{\text{scale},v}\big) \\
&\times \frac{1}{1 + \text{PAR}/\text{PAR}_{0,v}} \times \text{PAR} \times \text{EVI} + \alpha_v \\
&\times \max\big(T, T_{\text{low},v}\big) + \beta_v \big].
\end{aligned}
\tag{13}
$$

3.4 VPRM preprocessor for online flux calculation in mesoscale atmospheric transport models

Complementary to the direct calculation of carbon fluxes, *pyVPRM* can also be used as a preprocessor to generate input files for online flux calculation within mesoscale atmospheric models, such as the greenhouse gas module of the Weather Research and Forecasting (WRF-GHG/WRF-Chem) model

or ICON-ART. In this case, the fluxes are calculated using the 2 m temperature and shortwave radiation at the surface calculated within the atmospheric model. The procedure for the generation of the input files is similar to the procedure described in Sect. 3.3. The difference is that, instead of using Eq. (13) to calculate the CO_2 fluxes, the EVI and LSWI fields as well as the land cover map are regridded to match the input format of the atmospheric model. Overall, the VPRM preprocessor needs to create seven files: two containing the daily EVI and LSWI for each vegetation class, four with the annual minimum and maximum EVI and LSWI for each vegetation class, and one with the pixel-wise fraction of each vegetation class. In *pyVPRM*, the output files can be directly written from a VPRM preprocessor instance using the *to_wrf_output(.)* method. Figure 5 shows an example of the vegetation fractions for Europe using the Copernicus Dynamic Land Cover Collection 3 (Buchhorn et al., 2020) as input.

4 Estimating VPRM parameters for Sentinel-2, MODIS, and VIIRS

The full equation of the VPRM model, Eq. (13), contains four free parameters for each vegetation class: the quantum efficiency λ, the half saturation value of the photosynthetic activity PAR_0, and two parameters, α and β, describing a linear respiration model with temperature. Those parameters are required to calculate the carbon fluxes, whether VPRM is used offline or within the weather prediction/tracer transport model. To estimate those parameters, in situ CO_2 flux measurements from eddy-covariance towers are used. We show here an example of the fitting procedure for the European domain and provide an updated VPRM parameter set for Sentinel-2, MODIS, and VIIRS.

4.1 Flux tower selection

Several data collections provide harmonized eddy-covariance flux tower measurements for a collection of measurement sites. For example, the FLUXNET2015 data collection (Pastorello et al., 2020) provides global data for a total of 212 sites, but currently only up to the year 2015. On a continental level, AmeriFlux provides data for North and South America, the ICOS Carbon Portal (ICOS RI et al., 2023) provides data for Europe, and OzFlux provides data for Australia and New Zealand.

For our European application, we combine data from FLUXNET and ICOS covering the period between 2002 and 2022. An overview of the locations and ecosystem types of the various stations is given in Fig. 6. For the fit of the Sentinel-2 parameters, only sites with data after 2015 can be used. To be consistent with previous VPRM versions (Gerbig and Koch, 2021), we use only 1 year of flux tower data per site. The year is selected as the year within the data ac-
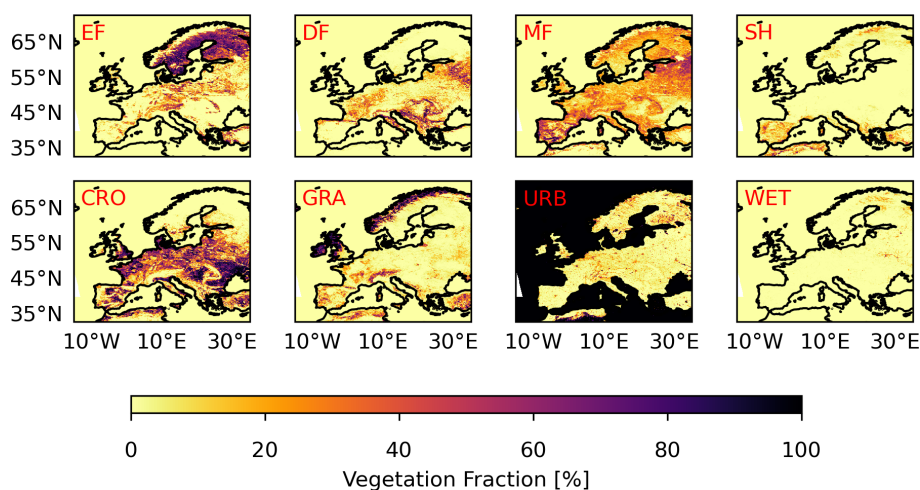
Figure 5. Vegetation fractions of the eight land cover classes used in our VPRM model, based on the Copernicus Dynamic Land Cover Collection 3. The data are regridded on a $0.25° \times 0.25°$ regular grid. This is a typical example of a vegetation fraction map that can also be used in mesoscale atmospheric models like WRF-GHG/WRF-Chem or ICON-ART. The abbreviations are evergreen forest (EF), deciduous forest (DF), mixed forest (MF), shrubland (SH), cropland (CRO), grassland (GRA), non-vegetated (URB), and wetland (WET). Not shown here are the other files generated by the *pyVPRM* preprocessor, i.e., the EVI and LSWI maps.
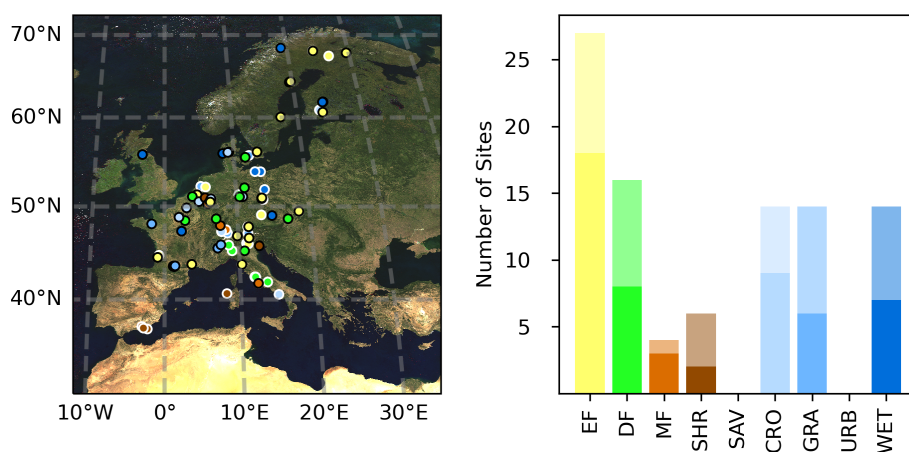
Figure 6. Left panel: the flux tower sites used to estimate the VPRM parameters. Circles with black and white contours indicate data that were used from the ICOS or FLUXNET data collection, respectively. Different colors show the different vegetation types with the number of sites shown in the histogram on the right. Brighter bars show the number of ICOS and FLUXNET stations with available data during the period covered by MODIS. Darker bars show the number of stations available since the launch of Sentinel-2. Abbreviations are as follows: EF – evergreen forest, DF – deciduous forest, MF – mixed forest, SHR – shrubland, CRO – cropland, GRA – grassland, WET – wetland, SAV – savanna. Background satellite image created using MODIS data.

quisition period of the respective satellite with the maximum amount of available flux tower data. Overall, we use 97 sites for MODIS, 52 sites for Sentinel-2, and 68 sites for VIIRS. An overview of the stations used for parameter estimation is shown in Sect. D for each satellite mission.

All flux towers use the eddy-covariance technique, which determines vertical fluxes from turbulence-resolving (i.e., sub-second) measurements of the vertical wind component and the quantity of interest – in our case, CO_2 (Baldocchi et al., 2001; Swinbank, 1951). They measure a weighted average of fluxes in the upwind direction. The spatial area from

which fluxes contribute to the measurement is called the footprint, and this depends strongly on the height above canopy of the flux tower itself, as well as other aerodynamic quantities such as the surface roughness (Chen et al., 2009; Schmid, 1994). Optimally, the flux tower should be surrounded by a sufficiently homogeneous landscape to be representative for a specific land cover class. This is, however, not always the case. For some sites, the measurement might see signals from different land cover types at different times (Järvi et al., 2012). Other sites might be located in a satellite pixel that overlaps with different land covers; see Fig. 2. For this rea-

son, we visually inspect all sites using Google Earth and remove those that are extremely heterogeneous on the spatial scale of the satellite resolution.

4.2 Spatial smoothing

Spatial smoothing is a way to account for footprints that exceed the size of a single satellite pixel. In previous VPRM versions (Mahadevan et al., 2008), the EVI and LSWI of the nine MODIS pixels surrounding the tower location were averaged for comparison with the flux tower data. This means averaging over a region of around $1.5 \times 1.5\,\text{km}^2$. In many cases, especially in Europe, the averaging is therefore done over heterogeneous land cover types, leading to inconsistencies between measured and modeled fluxes; see Fig. 10.

We mitigate this problem by dropping the spatial smoothing for MODIS and VIIRS (with $500\,\text{m}$ resolution), i.e., we use only the pixel in which the tower is located. For Sentinel-2, with a pixel size of $20\,\text{m}$, we use a 3×3 pixel ($60\,\text{m} \times 60\,\text{m}$) spatial smoothing centered at the tower location.

In general, *pyVPRM* also provides the option of using arbitrary weighting kernels in the *smearing(.)* function of the VPRM preprocessor to better match the satellite observation to flux tower footprint models.

4.3 Fitting VPRM parameters

For the fit, we choose only the highest-quality data points, thus removing low turbulence conditions with bad flux measurements (i.e., only using data where "*NEE_VUT_REF_QC*" is 0). Further, we ensure that the data are distributed uniformly over the year and the time of the day. To do that, we group the data in two dimensions by week of the year and time of the day in 3-hour time steps. Subsequently, we randomly sample three measurements from each group. This leads to a selection of $\mathcal{O}(10^3)$ data points with uniform distribution over the year for each tower. The selected data are fitted using a two-step mean-squared-error fitting. In the first step, the respiration parameters are fitted for nighttime data only, thus naturally removing the light-dependent photosynthesis. In the second step, NEE is fitted using the best-fit parameters of the first step for the respiration parameters. This fitting procedure hence does not require a partitioning of the measured NEE into GPP and respiration but rather uses the flux measurements directly. This avoids typical assumptions and uncertainties that arise when partitioning the carbon fluxes from eddy-covariance towers (Wutzler et al., 2018). In *pyVPRM*, each VPRM model class has a function *fit_vprm_data(.)* that performs the fit.

5 Results

VPRM parameters for the different satellite missions (MODIS, VIIRS, Sentinel-2) for the European domain are shown in Table 3. We observe that, although the wavelength bands of MODIS and Sentinel-2 largely overlap, there are some differences between the parameters for the two products. This could be related to slight differences in the satellite bands and data collection or in the different spatiotemporal resolutions of the observations. This question will be investigated in further studies. The parameters for VIIRS are calculated using EVI2 (without the blue band) and hence are not expected to be directly comparable.

In order to evaluate how the high resolution of Sentinel-2 can improve flux estimates, we have studied some of the (heterogeneous) cropland flux sites in more detail. In Fig. 7, the monthly average diurnal cycle is shown for the Selhausen Juelich site (DE-RuS; 50.8659° N, 6.4471° E). Evidently, the monthly median diurnal cycle of Sentinel-2 matches the observation much better than the one from MODIS in most months. This is a direct consequence of the different seasonal cycles of the EVI, as shown in Fig. 2. While the higher resolution of the Sentinel-2 images allows the growing periods of the specific field to be resolved, MODIS is averaging over several fields, resulting in a superposition of their seasonal cycles. This results in predicted fluxes in April and May that are much larger than what is observed at the site. Overall, the mean-squared deviation from the measurement reduces from 43.9 (MODIS) to 7.1 (Sentinel-2). Similar effects can be observed for many cropland sites, which is especially problematic in Europe, where 38 % of the land surface is covered with cropland. Figure 8 gives an overview of the mean-squared deviation from the measurement for the cropland sites with data availability during the Sentinel-2 mission. For comparison, we also show similar results for evergreen forest sites, which are usually pretty homogeneous (the same plot for deciduous and mixed forest is shown in the Appendix, Fig. G1). As expected, the majority of cropland sites show a significant reduction in the mean-square deviation, while there is no trend for evergreen forests (as for the other forest classes). The full diurnal cycles of all cropland sites in Fig. 8 are shown in Appendix E. Our findings are in line with a recent study of Bazzi et al. (2024) that found that using Sentinel-2 data significantly improves the simulation of cropland carbon dioxide fluxes in Europe.

As an example for a high-resolution *pyVPRM* flux, we have calculated hourly NEE in the $19\,\text{km} \times 19\,\text{km}$ region around Vienna using a combination of Sentinel-2 data for 2022, a hybrid land cover map (as explained above), and the ERA5-Land meteorological reanalysis data from the European Centre for Medium-Range Weather Forecasts (ECMWF) (Hersbach et al., 2020). For shortwave radiation, we use the parameter *ssrd* (surface solar radiation downwards; paramID:169), and for the $2\,\text{m}$ temperature, the parameter *t2m* ($2\,\text{m}$ temperature; paramID:167) (Muñoz Sabater et al., 2021). The VPRM parameters are those described later in Table 3. The monthly aggregated results for May, July and October are shown in Fig. 9.

Table 3. Overview of the VPRM parameter sets for MODIS, Sentinel-2, and VIIRS and the different ecosystems. Abbreviations are as follows: EF – evergreen forest, DF – deciduous forest, MF – mixed forest, SHR – shrubland, CRO – cropland, GRA – grassland, WET – wetland. The parameters of Gerbig (2024) can be found in Table C1 for comparison.

	Temperatures				MODIS				Sentinel-2				VIIRS			
	T_{min}	T_{opt}	T_{max}	T_{low}	λ	par_0	α	β	λ	par_0	α	β	λ	par_0	α	β
EF	-4	15	38	-3	0.13	561.8	0.21	1.09	0.12	566.7	0.23	1.25	0.13	518.3	0.24	1.11
DF	1	21	37	0	0.12	526.7	0.24	1.15	0.11	428.9	0.25	1.47	0.13	461.0	0.26	1.12
MF	-1	18	38	0	0.15	439.3	0.2	0.87	0.14	393.9	0.18	1.29	0.13	506.4	0.22	0.71
SHR	-1	19	44	2	0.1	440.2	0.08	0.59	0.29	216.8	0.16	0.99	0.08	565.0	0.15	0.44
CRO	-3	16	50	-3	0.09	925.0	0.17	1.10	0.08	965.8	0.17	1.14	0.08	930.5	0.18	1.17
GRA	-2	17	36	-2	0.23	414.9	0.33	1.29	0.17	607.8	0.34	1.12	0.23	483.1	0.36	1.08
WET	-2	26	40	0	0.12	393.2	0.28	-0.3	0.13	316.4	0.32	-0.39	0.09	552.8	0.29	-0.06
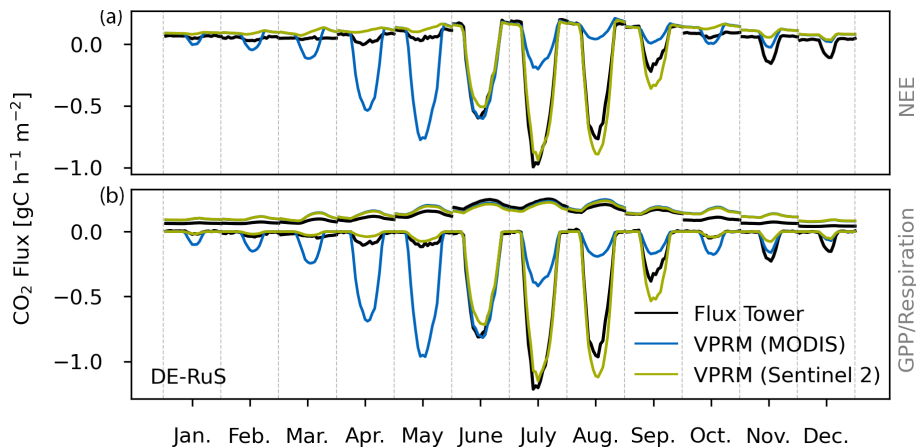
Figure 7. The mean diurnal cycle for each month at the cropland site Selhausen Juelich (DE-RuS, 50.8659° N; 6.4471° E) in 2022. The median tower measurements for each hour of the day are shown as black lines. Colored solid lines indicate the results from the VPRM model using indices from Sentinel-2 (green) and MODIS (blue). In the top panel, NEE is shown, and in the bottom panel, GPP (negative values, carbon uptake) and respiration (positive values, carbon release) are shown. The flux partitioning is based on the nighttime partitioning method with a variable u^* threshold (Reichstein et al., 2005).

Finally, we have compared the MODIS-based European fluxes from *pyVPRM* against those published on the ICOS Carbon Portal for the year 2023 (ICOS RI et al., 2023); see Fig. 12. A summary of the model properties for the different flux datasets is shown in Table 4. The plot on the left shows the annual net carbon flux as published on the ICOS Carbon Portal using the old software and old model settings. The middle panel shows a model run with the same VPRM parameters and the same land cover maps as the old version but using the *pyVPRM* to run the computations. The comparison shows that the old and new software frameworks produce numerically compatible results. The right panel shows the annual fluxes using *pyVPRM* and the new VPRM parameters as well as the new land cover map. This clearly shows how the fluxes change with the new approach.

6 Discussion

Evidently, fluxes change significantly with the new VPRM version. This is primarily driven by improvements in the VPRM parameter estimation for cropland and grassland. The origin of those improvements is illustrated in Fig. 10. Two changes are important here: one related to the spatial smoothing of the satellite data and one related to the fit procedure itself.

First, the old VPRM version used a 3×3 spatial smoothing of the MODIS data before the fit, while *pyVPRM* does not. The difference becomes particularly visible for heterogeneous land cover types – in Europe especially for grassland and cropland. Figure 10 shows an example of this for the Gebesee (DE-Geb; 51.0997° N, 10.9146° E) cropland site. A single MODIS pixel on top of the flux tower already covers more than one field. Consequently, doing a 3×3 pixel smoothing includes many fields, diluting the seasonal cycle of the EVI (see also Fig. 2). As a result, the new GPP model,
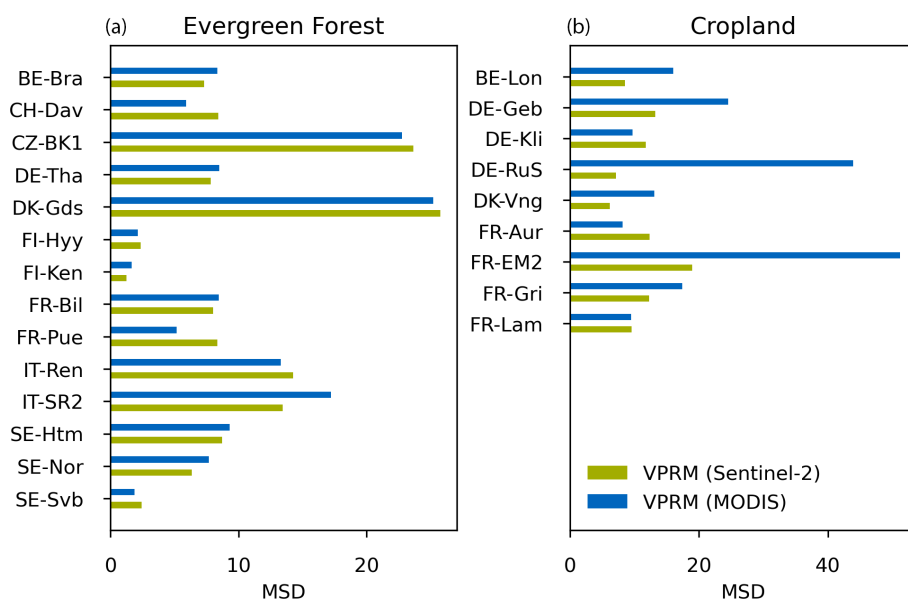
Figure 8. Mean squared deviation (MSD) between the VPRM prediction and the eddy flux tower observation for evergreen forest **(a)** and cropland **(b)** sites. Green and blue are used to show the VPRM predictions using Sentinel-2 and MODIS, respectively.
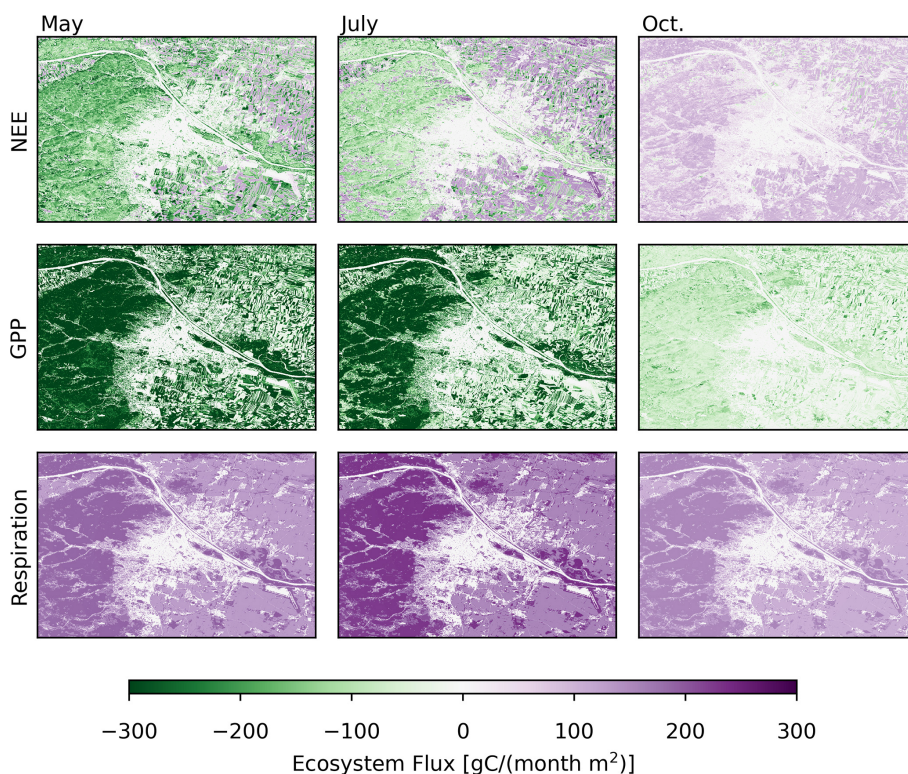

Figure 9. Monthly aggregated ecosystem fluxes for 3 months in the region around Vienna. The different months (May, July, October) are shown in the panels from left to right. From top to bottom, net ecosystem exchange (NEE), gross primary production (GPP), and respiration are shown. Negative values represent a carbon uptake, while positive fluxes show carbon release into the atmosphere. The fluxes are based on Sentinel-2 images, a hybrid land cover map, and hourly ERA5-Land meteorological data. The corresponding land cover map is shown in Fig. 4.

Table 4. A comparison of the VPRM settings used to estimate the European carbon fluxes in Fig. 12.

	ICOS Carbon Portal	*pyVPRM* (old model)	*pyVPRM* (new model)
Satellite product	MODIS MOD09A1 version 6.1	MODIS MOD09GA version 6.1	MODIS MOD09GA version 6.1
Land cover map	SYNMAP	SYNMAP	Copernicus Dynamic Land Cover Collection 3
Meteorology	ECMWF IFS (3-hourly)	ECMWF ERA5-Land (hourly)	ECMWF ERA5-Land (hourly)
VPRM parameters	VPRM optimization code version Rev.7 (using 3×3 pixel smoothing)	VPRM optimization code version Rev.7 (using 3×3 pixel smoothing)	*pyVPRM* v3.0 (no spatial smoothing)
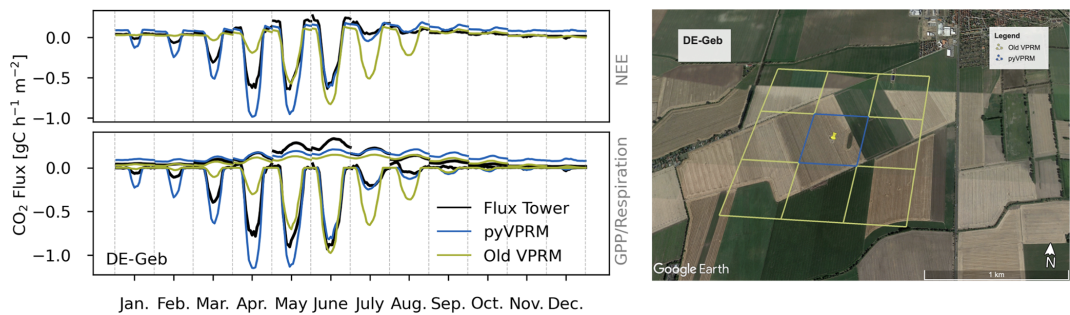
Figure 10. Left panel: the monthly mean diurnal cycles for NEE (top plot) and for respiration and GPP (bottom plot) for the cropland site Gebesee (DE-Geb; 51.0997° N, 10.9146° E) in 2007. Flux tower data are shown as solid black lines, and VPRM estimates from the old and new model are shown as green and blue lines, respectively. The flux partitioning is based on the nighttime partitioning method with a variable u^* threshold. GPP is shown as negative fluxes (carbon uptake), and respiration as positive values (carbon release). Right panel: image of the DE-Geb site. The blue square shows the MODIS pixel on top of the flux tower location (yellow pin). The green pixels show the satellite data used in the previous VPRM version. © Google Earth 2024.

which does not use spatial smoothing, better matches the observations (Fig. 10).

The second key difference between the versions is that the *pyVPRM* fit follows a two-step procedure: at the beginning, the respiration parameters are fitted against nighttime (respiration) measurements, and then the GPP parameters are fitted using (daytime) NEE data (utilizing the previously fitted respiration parameters). The old parameters, on the other hand, were produced by simultaneously fitting the GPP and respiration parameters at once using daytime and nighttime NEE data. The problem with this strategy is that errors in the GPP are propagated to the respiration, as GPP fluxes are much larger and more variable than those of respiration. In the case of Gebesee (DE-Geb; 51.0997° N, 10.9146° E), the underestimation of the GPP forces the respiration to also be underestimated to better match the NEE.

In summary, this shows that it is important to (1) match the spatial smoothing of the satellite data to the flux tower footprint and (2) to fit respiration and GPP separately to avoid systematic biases. As a consequence, the slope of the new respiration function, α in Eq. (9), is 3 times higher for grasslands and croplands than the previously reported parameters (Gerbig, 2024) and therefore much more in line with the respiration parameters for the other vegetation classes. Figure 11 shows the respiration function for the grasslands sites for the old and the new version of VPRM (the same plot for the cropland sites is shown in the Appendix, Fig. F1). The respiration function in the old version underestimates the carbon release to the atmosphere for most of the sites. The deviation becomes especially large for high-respiration periods (i.e., high-temperature periods). While it is evident that the simple linear respiration function does not capture all effects of the ecosystem respiration, the new function is clearly an improvement over the old version. This has large implications for European flux estimates, as croplands and grassland make up 39 % and 15 % of the total European land surface area, respectively (Buchhorn et al., 2020).

Overall the annual NEE budget for the European domain in 2023 changes by 75 %, from $-2.1\,\mathrm{PgC\,yr^{-1}}$ (ICOS Carbon Portal (Gerbig and Koch, 2024)) to $-0.45\,\mathrm{PgC\,yr^{-1}}$ (new *pyVPRM* estimate). The former is likely an overestimation of the carbon sink, caused by the underestimation of respiration. Our new *pyVPRM* budget, on the contrary, is more consistent with previous works estimating the European carbon sink (Monteil et al., 2020; Munassar et al., 2022; Crowell et al., 2019; Scholze et al., 2019). Monteil et al. (2020) provides a comprehensive intercomparison study of different inversion systems with varying transport models, inversion
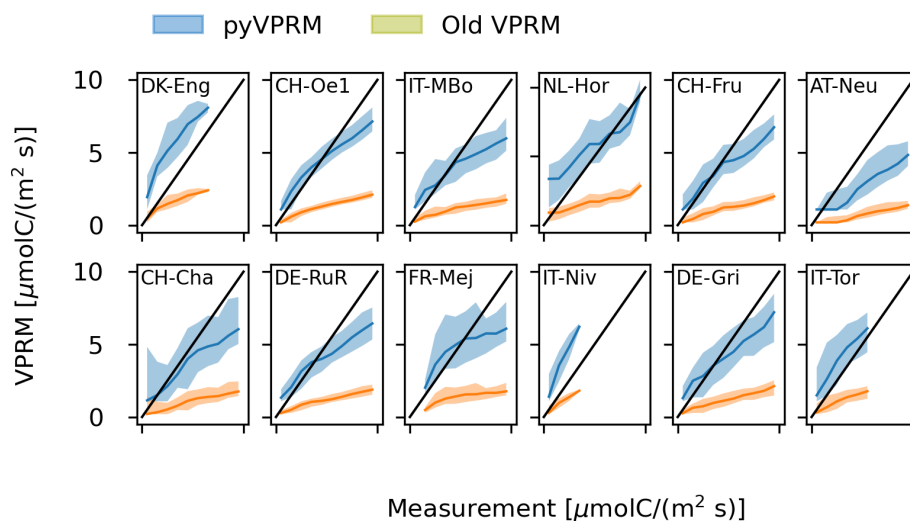
Figure 11. Comparison of VPRM respiration models and eddy-covariance measurements for the old VPRM model and the new *pyVPRM* model at the grassland sites. For the measurements data, the partitioned variable "*RECO_NT_VUT_REF*" has been used. The bands show the 10th and 90th percentiles of the model. The black solid line is the expectation for a perfect model.
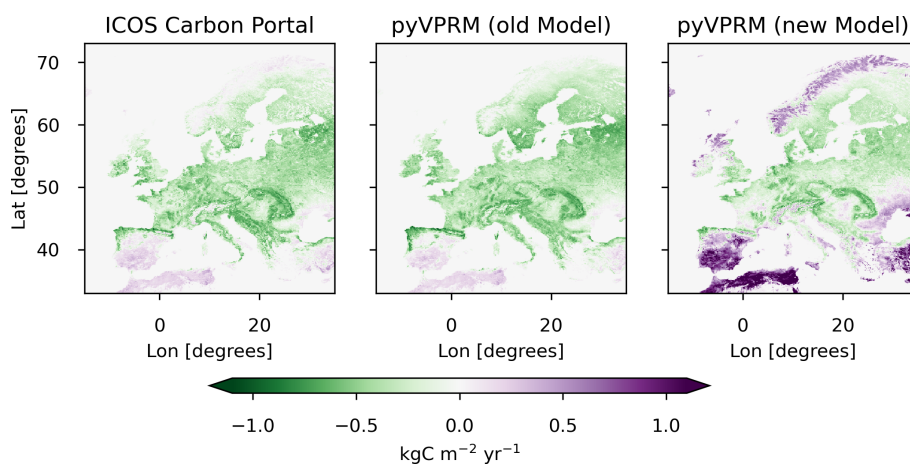

Figure 12. Annual NEE for Europe in 2023 at a 0.25° × 0.25° resolution. Negative flux values (green) show a net carbon uptake, while positive values (purple), a net carbon release. Left panel: fluxes taken from the ICOS Carbon Portal (Gerbig and Koch, 2024). Middle panel: fluxes generated with *pyVPRM* but using the same VPRM parameters and land cover map (SYNMAP) as for the fluxes in the ICOS Carbon Portal. Right panel: fluxes calculated using the new *pyVPRM* implementation with the new land cover map and MODIS VPRM parameters as given in Table 3.

approaches, and priors for the European domain. For most prior biogenic flux models, the estimate carbon sink is between -0.5 and $0 \, \mathrm{PgC \, yr^{-1}}$. A much larger sink is estimated only when using the old VPRM fluxes as the prior, which is likely related to the respiration issue discussed above. By assimilating three datasets (in situ atmospheric CO_2, remotely sensed soil moisture, and vegetation optical depth), Scholze et al. (2019) estimate a carbon sink of $-0.3 \pm 0.08 \, \mathrm{PgC \, yr^{-1}}$. Crowell et al. (2019) use OCO-2 XCO2 data in an inversion system and estimate the sink as $-0.25 \pm 0.46 \, \mathrm{PgC \, yr^{-1}}$.

As expected, the changes from the old to the new VPRM estimate are mainly driven by changes in the budget of grassland and cropland. In both cases, the carbon sink decreases by around $0.7 \, \mathrm{PgC \, yr^{-1}}$. Cropland is estimated to be a sink with $-0.16 \, \mathrm{PgC \, yr^{-1}}$. Grassland, on the contrary, turns into a source of around $0.4 \, \mathrm{PgC \, yr^{-1}}$. This is clearly visible in Scandinavia, around the Mediterranean, and in northern Africa. Assuming a closed carbon cycle, this is an indication that some model issues also remain in the new VPRM version. Especially unrealistic are net respiration fluxes in low soil and biomass carbon regions in southern Spain up to nearly $1 \, \mathrm{kgC \, m^2 \, yr^{-1}}$. As a second-order effect, the sink of evergreen forests is reduced by around $0.4 \, \mathrm{PgC \, yr^{-1}}$.

There are different limitations in the current VPRM model that could explain inaccuracies: (1) the sparse coverage of eddy-covariance towers, especially in Scandinavia, Spain, and the Balkans, does not provide strong constraints on the VPRM parameters in these regions. Hence, the VPRM parameters from central Europe are extrapolated to regions and climates where they likely have limited applicability. This problem appears to be smaller in the previous VPRM version because of the underfitted respiration parameters; see Fig. 11. (2) The linear respiration function is likely unrealistic for high temperatures and low soil moisture levels. Recent studies suggest that unimodal respiration functions might provide a better description under these conditions (Niu et al., 2024). (3) The respiration function currently does not take into account the total amount of plants and biomass available. This problem can be tackled by including EVI in the respiration as shown in (Gourdji et al., 2022). An implementation of this modified VPRM is available in the *pyVPRM* GitHub repository (https://github.com/tglauch/pyVPRM/tree/main, last access: 24 July 2025) but not discussed in this paper. Improvements for the respiration function will be investigated and implemented in future versions of *pyVPRM*. Finally, grasslands pose a special challenge, as they can be managed/unmanaged, xeric/non-xeric, and high/low altitude. Most European flux tower sites currently measure managed grasslands in central Europe. Adding flux towers in the dry (Mediterranean) and polar (Scandinavian) regions might facilitate calculation of the VPRM parameters for those different types of grasslands.

A central improvement of *pyVPRM* is the ability to use different satellite and land cover data products depending on the application. While MODIS and VIIRS provide long-term observations at 500 m resolution, Sentinel-2 is especially applicable for high-resolution applications like the modeling of urban fluxes. Especially for heterogeneous land cover types such as croplands and grasslands, the new VPRM parameters enhance the coherence between the model and flux tower data. However, the current VPRM parameter estimation still has limitations. Notably, it does not account for the time-dependent footprint of the flux towers, which remains a key area for improvement in future research.

7 Conclusions

pyVPRM provides a next-generation framework for the application of the Vegetation Photosynthesis and Respiration Model (VPRM) from city to continental scale. The model is driven by remote sensing indices and meteorological variables to estimate the ecosystem's light-use efficiency for the uptake of carbon through photosynthesis and the (temperature-dependent) ecosystem respiration. Typical applications are the estimation of ecosystem carbon budgets from city to global scale and as a biospheric prior for the estimation of both biogenic and anthropogenic CO_2 emissions using atmospheric inversion with transport models like WRF-GHG (Beck et al., 2012) or ICON-ART (Schröter et al., 2018).

pyVPRM extends previous VPRM versions (Mahadevan et al., 2008) by including the latest remote sensing products from Sentinel-2 and VIIRS, as well as updated and dynamic land cover products like the global Copernicus Dynamic Land Cover Collection 3 and the global ESA WorldCover. Using Sentinel-2 data enables us, for the first time, to resolve very heterogeneous landscapes like croplands, agricultural grasslands, or urban areas. Using VIIRS as a replacement for MODIS guarantees consistent long-term datasets after the planned discontinuation of MODIS. Furthermore, *pyVPRM* brings improvements in the model parameterization of grasslands and shrublands compared to the current implementation in the ICOS Carbon Portal (Gerbig, 2024).

Free model parameters for eight ecosystem types are fitted using data from up to 97 eddy-covariance towers across Europe. Comparing to flux tower data we observe significant improvements with the Sentinel-2 model, due to a better representation of the flux tower footprint. This is most important for cropland and grassland sites, which are heterogeneous vegetation classes that are very abundant in Europe.

In contrast to previous MODIS-based flux estimates for the European domain (Gerbig and Koch, 2021), *pyVPRM* has a more realistic overall budget when compared to independent top-down estimates (Monteil et al., 2020) and improves the seasonal and diurnal cycle for grassland and cropland. This is mostly related to the improved fitting procedure, in which the estimation of the respiration function is not influenced by mismatches between the measured GPP and the EVI estimation. Smaller improvements come from the usage of a higher-resolution land cover map and the replacement of the 3-hourly ECMWF IFS model (Roberts et al., 2018) with the hourly and higher-resolution ERA5-Land reanalysis (Muñoz Sabater et al., 2021).

Due to its modular structure, *pyVPRM* can be easily extended to incorporate other satellite missions, meteorological models, and land cover classifications. Likewise, different versions of the VPRM model can be implemented, e.g., the modified VPRM that includes nonlinear respiration terms (Gourdji et al., 2022) or the urban VPRM, which has been optimized for applications inside of urban areas (Hardiman et al., 2017). Likewise, we can use the *pyVPRM* framework to run machine-learning-based models.

Appendix A: Code structure

For examples on how *pyVPRM* can be used, hands-on example scripts are available on GitHub (https://github.com/tglauch/pyVPRM_examples/tree/main, last access: 24 July 2025). Here, we provide a brief overview of the classes and scripts provided within *pyVPRM*. Two main libraries provide the interface for accessing and preprocessing

the required meteorological and satellite data: *pyVPRM/meteorologies* and *pyVPRM/sat_managers*), respectively. The main preprocessing of the satellite data and land cover maps is done in the VPRM class, defined in *VPRM.py*. This is necessary for any kind of VPRM usage. The modules of different VPRM flux models and parameter-fitting functions are defined in the scripts in *pyVPRM/vprm_models/*, such as *pyVPRM/vprm_models/vprm_base.py* for the "base" version of the model. The interface to work with flux tower data used for parameter fitting is given in *pyVPRM/lib/flux_tower_class.py*, and some useful functions are provided in *pyVPRM/lib/functions.py*. More details about the *scripts/libraries* and the functions therein are provided below.

A1 *pyVPRM/meteorologies*

The *met_data_handler* classes in this folder provide an interface for the input meteorological data, which need to be customized if using a different model or data source. All meteorology classes are derived from the base class in *met_base_class.py*. An example to implement a new meteorology class can be found in *era5_class_draft.py*. *met_local_measurement.py* is used to extract and employ site-level meteorological data.

A2 *pyVPRM/sat_managers*

The *satellite_data_manager* class in this library is the basic data structure for all satellite image and land cover maps used in *pyVPRM*. It provides functions to re-project, transform, merge, and crop satellite images. All other classes for specific satellite images or land cover maps, with their respective loading routines, are derived from this base class and implemented in the respective class files in the folder.

The other scripts in this library define classes for specific satellite reflectance products (*modis.py*, *proba_v.py*, *sentinel2.py*, *viirs.py*, *viirs09ga.py*) or land cover maps (*city.py*, *copernicus.py*, *esa_world_cover.py*, *mapbiomas.py*, *synmap.py*), along with product-specific functions for data screening (e.g., for clouds, snow, and bad pixels). Configuration (YAML) files defining the VPRM vegetation classes for different land cover maps are found in *pyVPRM/vprm_configs* and are required to map the land cover categories to VPRM classes.

A3 *VPRM.py*

The VPRM class defined in *VPRM.py* is the implementation of the VPRM preprocessor. This is the central code to calculate the satellite indices, run the time smoothing, transform satellite data and the land cover map to the same grid, and prepare all the variables for the VPRM models. It can also be used to generate input files to run VPRM online in atmospheric models. In order to run the preprocessor, a configuration file with a mapping from land cover classes to VPRM classes is required.

A4 *pyVPRM/vprm_models/vprm_base.py*

In this folder, different implementations of the VPRM model are included. Every implementation requires at least a function to fit the VPRM parameters and make VPRM predictions given an instance of the VPRM preprocessor and the meteorology. The version described throughout this paper is in *vprm_base.py*.

A5 *pyVPRM/lib/flux_tower_class.py*

Flux tower data are not completely harmonized in terms of format, and as such, custom classes will likely need to be added to accommodate new data sources, and vegetation classes/land cover types may need to be harmonized by hand. Custom classes are included in this script already for FLUXNET, ICOS, AmeriFlux, and the LBA-ECO CD-32 Flux Tower Network Data Compilation. This can also be used as a template for adding new flux tower sites.

pyVPRM/lib/functions.py

Additional functions that are used in *pyVPRM* are stored in *functions.py*.

Appendix B: Data quality masking

Table B1. Flags used for data masking in MODIS. Scenes where any of the band quality, cloud masking, or cloud shadow masking criteria are not fulfilled are masked out. Scenes with an active snow flag receive special treatment; see Sect. 3.1.3.

	MODIS
Band quality masking	Highest-quality surface reflectance band quality description (0000) for band 1, band 2, band 3, band 6
Cloud masking	State QA flag 0–1 (cloud state) $==00$ (clear), and state QA flag 8–9 (cirrus detected) $==00$ (none)
Cloud shadow masking	State QA flag 2 (cloud shadow) $==0$ (no)
Snow masking	State QA flag 12 (MOD35 snow/ice flag) $==0$ (no)

Table B2. Flags used for data masking in VIIRS. Scenes where any of the band quality, cloud masking, or cloud shadow masking criteria are not fulfilled are masked out. Scenes with an active snow flag receive special treatment; see Sect. 3.1.3.

	VIIRS
Band quality masking	Highest-quality surface reflectance band quality description (0000) for band 1, band 2, band 3
Cloud masking	State QA flag 0–1 (cloud state) $==00$ (clear), and state QA flag 8–9 (cirrus detected) $==00$ (none)
Cloud shadow masking	State QA flag 2 (cloud shadow) $==0$ (no)
Snow masking	State QA flag 12 (MOD35 snow/ice flag) $==0$ (no)

Table B3. Flags used for data masking in Sentinel-2. Scenes where any of the band quality, cloud masking, or cloud shadow masking criteria are not fulfilled are masked out. Scenes with an active snow flag receive special treatment; see Sect. 3.1.3.

	Sentinel-2
Band quality masking	SCL flag not 0, 1, 2
Cloud masking	SCL flag not 8, 9, 10
Cloud shadow masking	SCL flag not 3
Snow masking	SCL flag not 11

Appendix C: Old VPRM parameters

Table C1. Overview of the VPRM parameter sets for MODIS used for the fluxes in the ICOS Carbon Portal (Gerbig, 2024). Abbreviations are as follows: EF – evergreen forest, DF – deciduous forest, MF – mixed forest, SHR – shrubland, SAV – Savanna, CRO – cropland, GRA – grassland.

	Temperatures				MODIS			
	T_{min}	T_{opt}	T_{max}	T_{low}	λ	par_0	α	β
EF	0	20	40	4	0.1	621.7	0.22	−0.64
DF	0	20	40	0	0.09	620.4	0.13	1.14
MF	0	20	40	2	0.07	1019.8	0.17	0.01
SHR	2	20	40	4	0.1	200.0	0.05	−0.17
SAV	2	20	40	0	0.06	344.4	0.005	0
CRO	5	22	40	0	0.04	2619.7	0.07	0.58
GRA	2	18	40	0	0.09	1147.4	0.09	0.36

Appendix D: Flux tower data

Table D1. Overview of flux tower sites and years used for estimating the VPRM parameters for MODIS, VIIRS, and Sentinel-2. Table 1/3.

Site name	Veg. type	Longitude [°E]	Latitude [°N]	MODIS	Sentinel-2	VIIRS
AT-Neu	GRA	11.32	47.12	2010	–	–
BE-Bra	EF	4.52	51.31	2022	2022	2022
BE-Lcr	DF	3.85	51.11	2020	2020	2020
BE-Lon	CRO	4.75	50.55	2020	2020	2020
BE-Maa	SH	5.63	50.98	2022	2022	2022
BE-Vie	MF	6.00	50.30	2022	2022	2022
CH-Cha	GRA	8.41	47.21	2013	–	2013
CH-Dav	EF	9.86	46.82	2022	2022	2022
CH-Fru	GRA	8.54	47.12	2008	–	2013
CH-Lae	MF	8.36	47.48	2014	–	2014
CH-Oe1	GRA	7.73	47.29	2007	–	–
CH-Oe2	CRO	7.73	47.29	2009	–	2013
CZ-BK1	EF	18.54	49.50	2022	2022	2022
CZ-BK2	GRA	18.54	49.49	2004	–	–
CZ-Lnz	DF	16.95	48.68	2022	2022	2022
CZ-wet	WET	14.77	49.02	2020	2020	2020
DE-Akm	WET	13.68	53.87	2010	–	2013
DE-Geb	CRO	10.91	51.10	2021	2021	2021
DE-Gri	GRA	13.51	50.95	2021	2021	2021
DE-Hai	DF	10.45	51.08	2020	2020	2020
DE-Har	MF	7.60	47.93	2021	2021	2021
DE-HoH	DF	11.22	52.09	2022	2022	2022
DE-Kli	CRO	13.52	50.89	2020	2020	2020
DE-Lkb	EF	13.30	49.10	2011	–	–
DE-Lnf	DF	10.37	51.33	2008	–	–
DE-Msr	EF	11.46	47.81	2021	2021	2021
DE-Obe	EF	13.72	50.79	2012	–	–
DE-RuR	GRA	6.30	50.62	2015	2020	2015
DE-RuS	CRO	6.45	50.87	2022	2022	2022
DE-RuW	EF	6.33	50.50	2012	2020	2012
DE-Seh	CRO	6.45	50.87	2009	–	–

Table D2. Overview of flux tower sites and years used for estimating the VPRM parameters for MODIS, VIIRS, and Sentinel-2. Table 2/3.

Site name	Veg. type	Latitude [°N]	Longitude [°E]	MODIS	Sentinel-2	VIIRS
DE-SfN	WET	11.33	47.81	2014	–	2014
DE-Spw	WET	14.03	51.89	2012	–	–
DE-Tha	EF	13.57	50.96	2022	2022	2022
DE-Zrk	WET	12.89	53.88	2014	–	2014
DK-Eng	GRA	12.19	55.69	2006	–	–
DK-Fou	CRO	9.59	56.48	2005	–	–
DK-Gds	EF	9.33	56.07	2021	2021	2021
DK-Skj	WET	8.40	55.91	2022	2022	2022
DK-Sor	DF	11.64	55.49	2022	2022	2022
DK-Vng	CRO	9.16	56.04	2022	2022	2022
ES-Amo	SH	−2.25	36.83	2009	–	–
ES-LJu	SH	−2.75	36.93	2009	–	2013
ES-LgS	SH	−2.97	37.10	2008	–	–
ES-Ln2	SH	−3.48	36.97	2009	–	–
FI-Hyy	EF	24.29	61.85	2019	2019	2019
FI-Jok	CRO	23.51	60.90	2001	–	–
FI-Ken	EF	24.24	67.99	2020	2020	2020
FI-Let	EF	23.96	60.64	2017	2017	2017
FI-Lom	WET	24.21	68.00	2008	–	–
FI-Sii	WET	24.19	61.83	2019	2019	2019
FI-Sod	EF	26.64	67.36	2011	–	2013
FI-Var	EF	29.61	67.75	2018	–	2018
FR-Aur	CRO	1.11	43.55	2021	2021	2021
FR-Bil	EF	−0.96	44.49	2022	2022	2022
FR-EM2	CRO	3.02	49.87	2020	2020	2020
FR-Fon	DF	2.78	48.48	2020	2020	2020
FR-Gri	CRO	1.95	48.84	2022	2022	2022
FR-Hes	DF	7.06	48.67	2022	2022	2022
FR-LBr	EF	−0.77	44.72	2002	–	–
FR-LGt	WET	2.28	47.32	2020	2020	2020
FR-Lam	CRO	1.24	43.50	2022	2022	2022
FR-Mej	GRA	−1.80	48.12	2020	2020	2020
FR-Pue	EF	3.60	43.74	2022	2022	2022
FR-Tou	GRA	1.37	43.57	2020	2020	2020
IT-BCi	CRO	14.96	40.52	2007	–	2013

Table D3. Overview of flux tower sites and years used for estimating the VPRM parameters for MODIS, VIIRS, and Sentinel-2. Table 3/3.

Site name	Veg. type	Latitude [°N]	Longitude [°E]	MODIS	Sentinel-2	VIIRS
IT-BFt	DF	10.74	45.20	2021	2021	2021
IT-CA1	DF	12.03	42.38	2012	–	–
IT-CA2	CRO	12.03	42.38	2012	–	–
IT-CA3	DF	12.02	42.38	2013	–	2013
IT-Col	DF	13.59	41.85	2014	–	2014
IT-Cp2	MF	12.36	41.70	2022	2022	2022
IT-Cpz	EF	12.38	41.71	2000	–	–
IT-Isp	DF	8.63	45.81	2014	–	2014
IT-La2	EF	11.29	45.95	2001	–	–
IT-Lav	EF	11.28	45.96	2013	–	2013
IT-Lsn	SH	12.75	45.74	2018	2018	2018
IT-MBo	GRA	11.05	46.01	2007	–	–
IT-Niv	GRA	7.14	45.49	2020	2020	2020
IT-Noe	SH	8.15	40.61	2010	–	–
IT-PT1	DF	9.06	45.20	2003	–	–
IT-Ren	EF	11.43	46.59	2022	2022	2022
IT-Ro1	DF	11.93	42.41	2006	–	–
IT-Ro2	DF	11.92	42.39	2009	–	–
IT-SR2	EF	10.29	43.73	2021	2021	2021
IT-SRo	EF	10.28	43.73	2004	–	–
IT-Tor	GRA	7.58	45.84	2022	2022	2022
NL-Hor	GRA	5.07	52.24	2007	–	–
NL-Loo	EF	5.74	52.17	2006	–	–
SE-Deg	WET	19.56	64.18	2020	2020	2020
SE-Htm	EF	13.42	56.10	2022	2022	2022
SE-Nor	EF	17.48	60.09	2020	2020	2020
SE-St1	WET	19.05	68.35	2013	–	2013
SE-Sto	WET	19.05	68.36	2022	2022	2022
SE-Svb	EF	19.77	64.26	2020	2020	2020
SJ-Adv	WET	15.92	78.19	2011	–	2013
UK-AMo	WET	−3.24	55.79	2022	2022	2022

Appendix E: Diurnal cycles for cropland sites
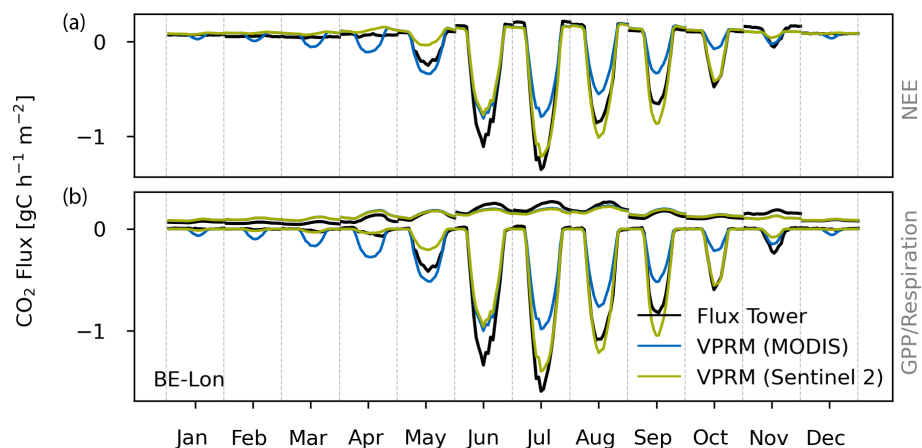
Figure E1. The mean diurnal cycle for each month at the cropland site BE-Lon. The median tower measurements for each hour of the day are shown as black lines. Colored solid lines indicate the results from the VPRM model using indices from Sentinel-2 (green) and MODIS (blue). In panel **(a)**, NEE is shown, and in panel **(b)**, GPP (negative values, carbon uptake) and respiration (positive values, carbon release) are shown. The flux partitioning is based on the nighttime partitioning method with a variable u^* threshold (Reichstein et al., 2005).
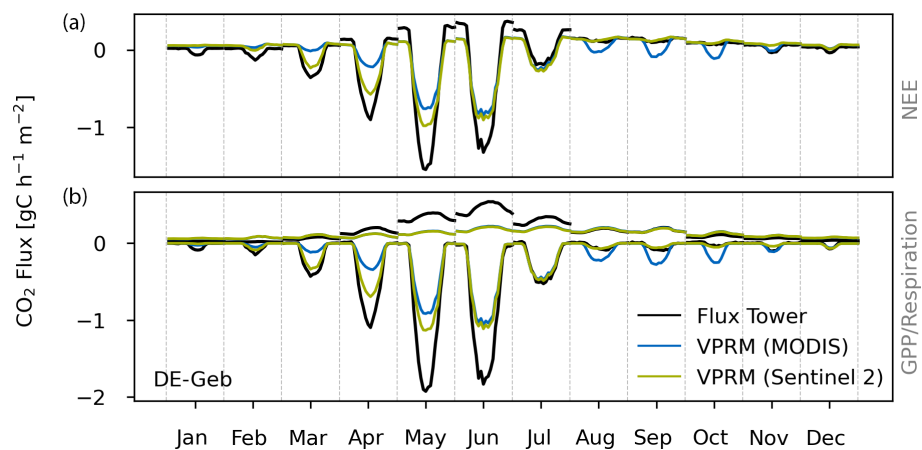
Figure E2. The mean diurnal cycle for each month at the cropland site DE-Geb. For more details, see Fig. E1.
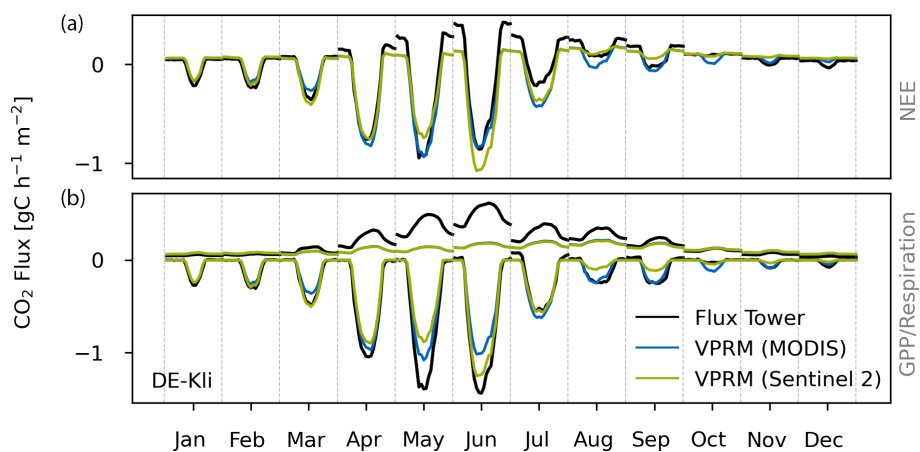
Figure E3. The mean diurnal cycle for each month at the cropland site DE-Kli. For more details, see Fig. E1.
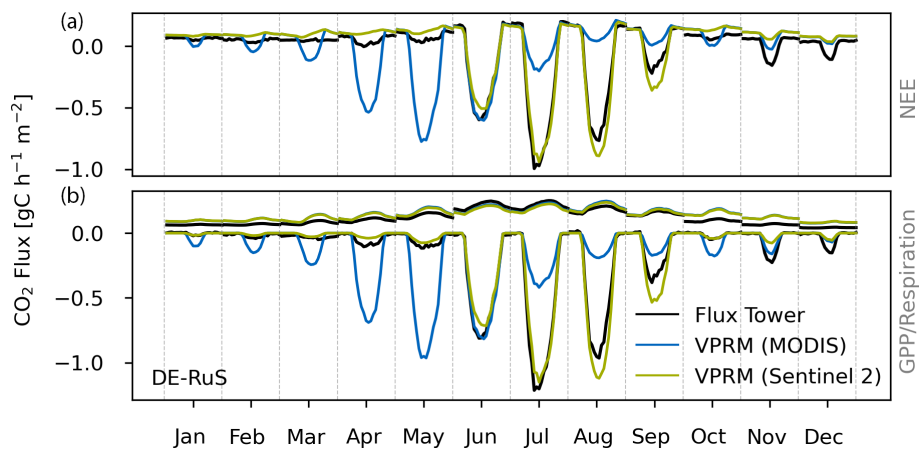
Figure E4. The mean diurnal cycle for each month at the cropland site DE-RuS. For more details, see Fig. E1.
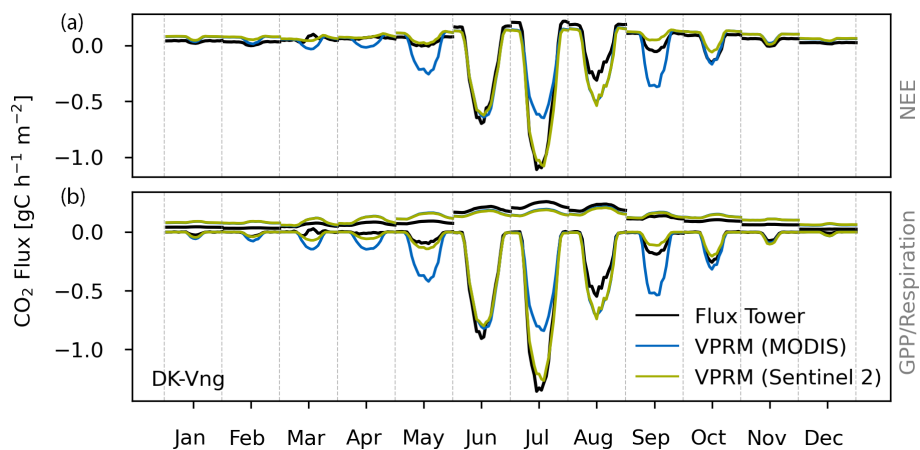
Figure E5. The mean diurnal cycle for each month at the cropland site DK-Vng. For more details, see Fig. E1.
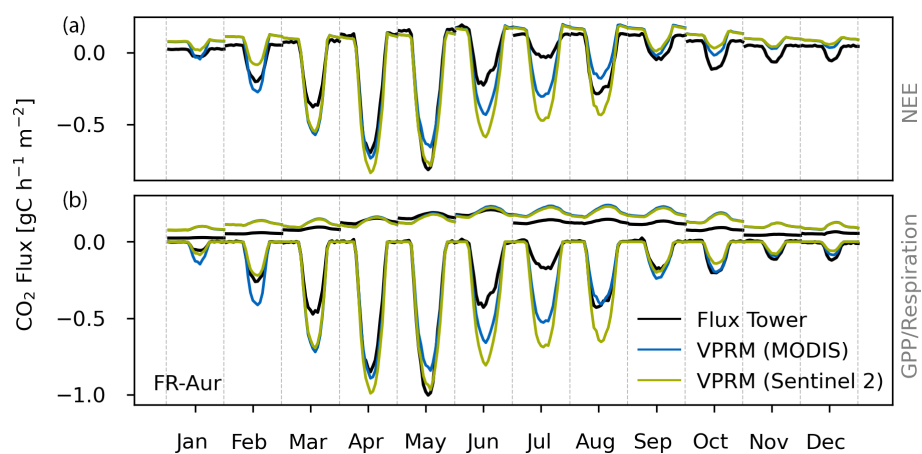
Figure E6. The mean diurnal cycle for each month at the cropland site FR-Aur. For more details, see Fig. E1.
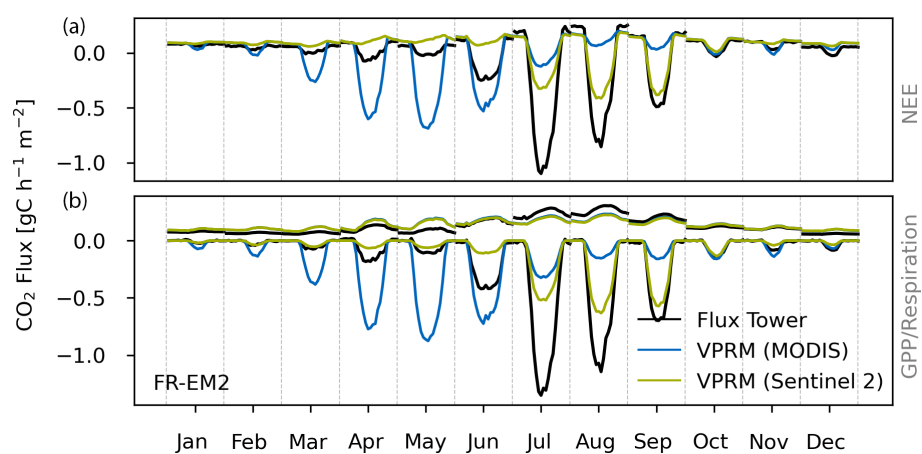
Figure E7. The mean diurnal cycle for each month at the cropland site FR-EM2. For more details, see Fig. E1.
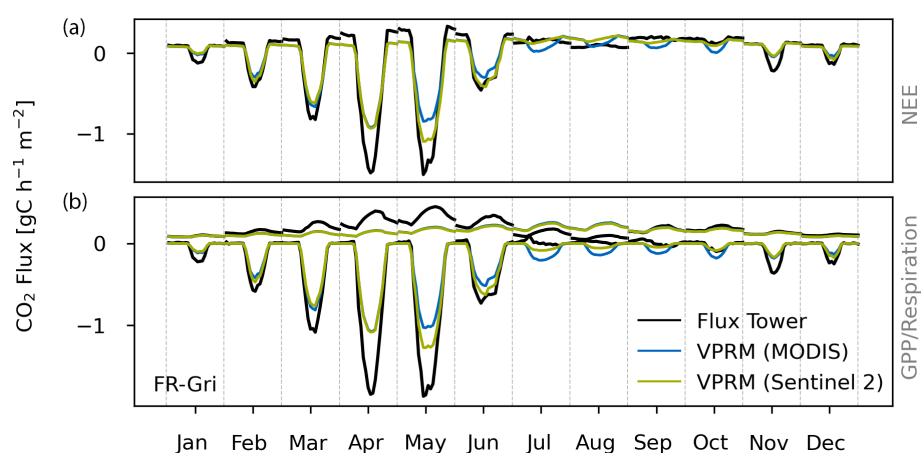
Figure E8. The mean diurnal cycle for each month at the cropland site FR-Gri. For more details, see Fig. E1.
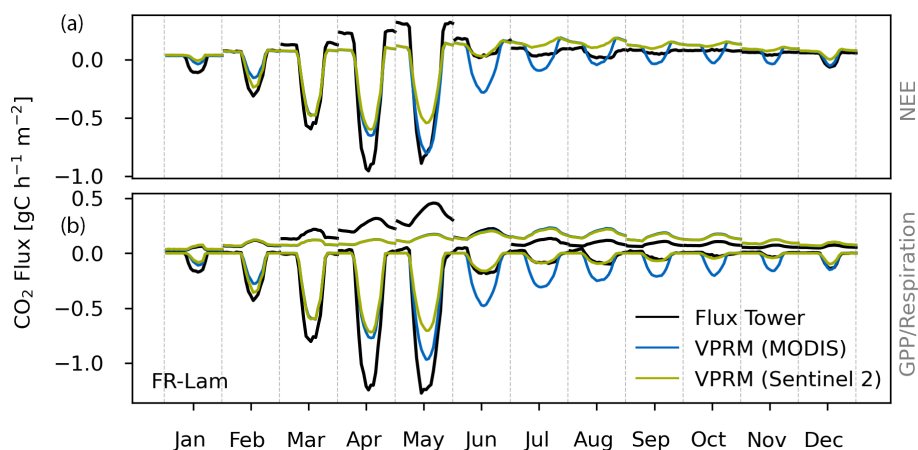
Figure E9. The mean diurnal cycle for each month at the cropland site FR-Lam. For more details, see Fig. E1.

Appendix F: Respiration functions
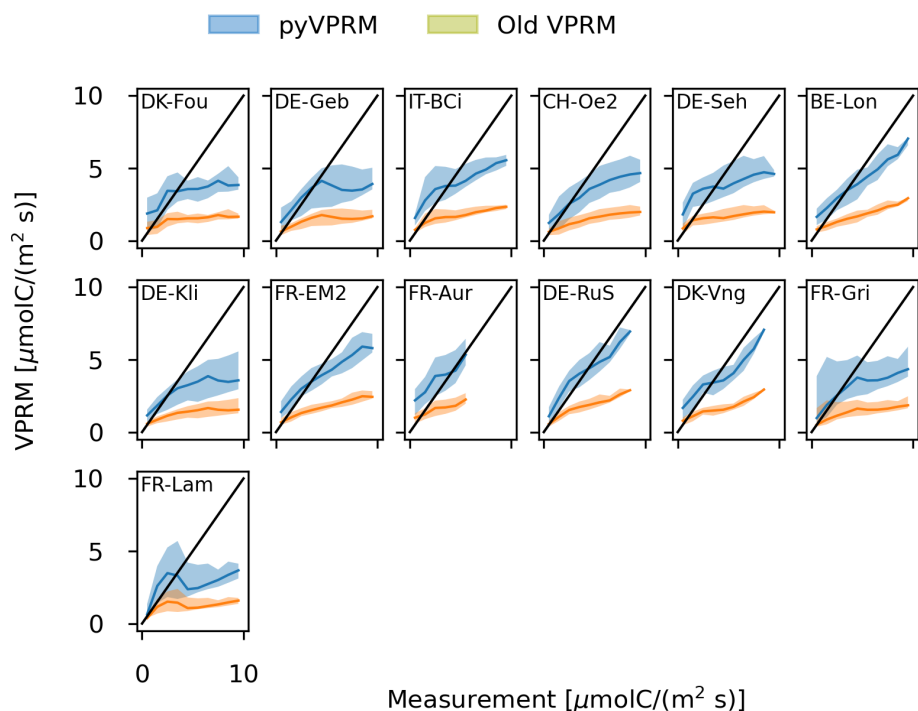
Figure F1. Comparison of VPRM respiration models and eddy-covariance measurements for the old VPRM model and the new *pyVPRM* model at the cropland sites. For the measurement data, the partitioned variable "*RECO_NT_VUT_REF*" has been used. The bands show the 10th and 90th percentiles of the model. The black solid line is the expectation for a perfect model.

Appendix G:　Mean squared deviation for deciduous forest and mixed forest
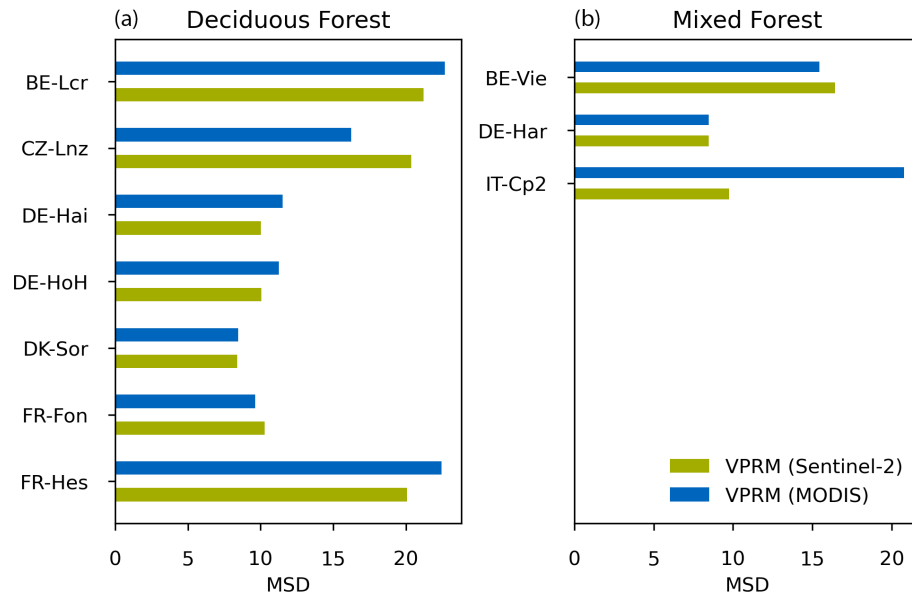
Figure G1. Mean squared deviation (MSD) between the VPRM prediction and the eddy flux tower observation for deciduous forest **(a)** and mixed forest **(b)** sites. Green and blue are used to show the VPRM predictions using Sentinel-2 and MODIS, respectively.

References

Ahmadov, R., Gerbig, C., Kretschmer, R., Körner, S., Rödenbeck, C., Bousquet, P., and Ramonet, M.: Comparing high resolution WRF-VPRM simulations and two global CO_2 transport models with coastal tower measurements of CO_2, Biogeosciences, 6, 807–817, https://doi.org/10.5194/bg-6-807-2009, 2009.

Baldocchi, D., Falge, E., Gu, L., Olson, R., Hollinger, D., Running, S., Anthoni, P., Bernhofer, C., Davis, K., Evans, R., Fuentes, J., Goldstein, A., Katul, G., Law, B., Lee, X., Malhi, Y., Meyers, T., Munger, W., Oechel, W., Paw U, K. T., Pilegaard, K., Schmid, H., Valentini, R., Verma, S., Vesala, T., Wilson, K., and Wofsy, S.: FLUXNET: A new tool to study the temporal and spatial variability of ecosystem-scale carbon dioxide, water vapor, and energy flux densities, B. Am. Meteorol. Soc., 82, 2415–2434, https://doi.org/10.1175/1520-0477(2001)082<2415:FANTTS>2.3.CO;2, 2001.

Bazzi, H., Ciais, P., Abbessi, E., Makowski, D., Santaren, D., Ceschia, E., Brut, A., Tallec, T., Buchmann, N., Maier, R., Acosta, M., Loubet, B., Buysse, P., Léonard, J., Bornet, F., Fayad, I., Lian, J., Baghdadi, N., Segura Barrero, R., Brümmer, C., Schmidt, M., Heinesch, B., Mauder, M., and Gruenwald, T.: Assimilating Sentinel-2 data in a modified vegetation photosynthesis and respiration model (VPRM) to improve the simulation of croplands CO_2 fluxes in Europe, Int. J. Appl. Earth Obs. Geoinf., 127, 103666, https://doi.org/10.1016/j.jag.2024.103666, 2024.

Beck, V., Koch, T., Kretschmer, R., Marshall, J., Ahmadov, R., Gerbig, C., Pillai, D., and Heimann, M.: The WRF Greenhouse Gas Model (WRF-GHG), Technical Report No. 25, Max Planck Institute for Biogeochemistry, Jena, Germany, https://www.bgc-jena.mpg.de/5363366/tech_report25.pdf (last access: 24 July 2025), 2012.

Bousquet, P., Ciais, P., Peylin, P., Ramonet, M., and Monfray, P.: Inverse modeling of annual atmospheric CO_2 sources and sinks: 1. Method and control inversion, J. Geophys. Res.-Atmos., 104, 26161–26178, 1999.

Buchhorn, M., Smets, B., Bertels, L., De Roo, B., Lesiv, M., Tsendbazar, N., Li, L., and Tarko, A.: Copernicus Global Land Service: Land Cover 100 m: Version 3 Globe 2015–2019: Product User Manual, Zenodo [data set], https://doi.org/10.5281/zenodo.3938963, 2020.

Chen, B., Black, T. A., Coops, N. C., Hilker, T., Trofymow, J., and Morgenstern, K.: Assessing tower flux footprint climatology and scaling between remotely sensed and eddy covariance measurements, Bound.-Lay. Meteorol., 130, 137–167, 2009.

Choulga, M., Janssens-Maenhout, G., Super, I., Solazzo, E., Agusti-Panareda, A., Balsamo, G., Bousserez, N., Crippa, M., Denier van der Gon, H., Engelen, R., Guizzardi, D., Kuenen, J., McNorton, J., Oreggioni, G., and Visschedijk, A.: Global anthropogenic CO_2 emissions and uncertainties as a prior for Earth system modelling and data assimilation, Earth Syst. Sci. Data, 13, 5311–5335, https://doi.org/10.5194/essd-13-5311-2021, 2021.

Cleveland, W. S.: Robust Locally Weighted Regression and Smoothing Scatterplots, J. Am. Stat. Assoc., 74, 829–836, https://doi.org/10.1080/01621459.1979.10481038, 1979.

Commane, R., Lindaas, J., Benmergui, J., Luus, K. A., Chang, R. Y.-W., Daube, B. C., Euskirchen, E. S., Henderson, J. M., Karion, A., Miller, J. B., Miller, S. M., Parazoo, N. C., Randerson, J. T., Sweeney, C., Tans, P., Thoning, K., Veraverbeke, S., Miller, C. E., and Wofsy, S. C.: Carbon dioxide sources from Alaska driven by increasing early winter respiration from Arctic tundra, P. Natl. Acad. Sci. USA, 114, 5361–5366, https://doi.org/10.1073/pnas.1618567114, 2017.

Crowell, S., Baker, D., Schuh, A., Basu, S., Jacobson, A. R., Chevallier, F., Liu, J., Deng, F., Feng, L., McKain, K., Chatterjee, A., Miller, J. B., Stephens, B. B., Eldering, A., Crisp, D., Schimel, D., Nassar, R., O'Dell, C. W., Oda, T., Sweeney, C., Palmer, P. I., and Jones, D. B. A.: The 2015–2016 carbon cycle as seen from OCO-2 and the global in situ network, Atmos. Chem. Phys., 19, 9797–9831, https://doi.org/10.5194/acp-19-9797-2019, 2019.

Dayalu, A., Munger, J. W., Wofsy, S. C., Wang, Y., Nehrkorn, T., Zhao, Y., McElroy, M. B., Nielsen, C. P., and Luus, K.: Assessing biotic contributions to CO_2 fluxes in northern China using the Vegetation, Photosynthesis and Respiration Model (VPRM-CHINA) and observations from 2005 to 2009, Biogeosciences, 15, 6713–6729, https://doi.org/10.5194/bg-15-6713-2018, 2018.

ESA: Sentinel-2 MSI Level-2A BOA Reflectance, ESA [data set], https://doi.org/10.5270/s2_-znk9xsj, 2022.

Friedlingstein, P., O'Sullivan, M., Jones, M. W., Andrew, R. M., Bakker, D. C. E., Hauck, J., Landschützer, P., Le Quéré, C., Luijkx, I. T., Peters, G. P., Peters, W., Pongratz, J., Schwingshackl, C., Sitch, S., Canadell, J. G., Ciais, P., Jackson, R. B., Alin, S. R., Anthoni, P., Barbero, L., Bates, N. R., Becker, M., Bellouin, N., Decharme, B., Bopp, L., Brasika, I. B. M., Cadule, P., Chamberlain, M. A., Chandra, N., Chau, T.-T.-T., Chevallier, F., Chini, L.

P., Cronin, M., Dou, X., Enyo, K., Evans, W., Falk, S., Feely, R. A., Feng, L., Ford, D. J., Gasser, T., Ghattas, J., Gkritzalis, T., Grassi, G., Gregor, L., Gruber, N., Gürses, O., Harris, I., Hefner, M., Heinke, J., Houghton, R. A., Hurtt, G. C., Iida, Y., Ilyina, T., Jacobson, A. R., Jain, A., Jarníková, T., Jersild, A., Jiang, F., Jin, Z., Joos, F., Kato, E., Keeling, R. F., Kennedy, D., Klein Goldewijk, K., Knauer, J., Korsbakken, J. I., Körtzinger, A., Lan, X., Lefèvre, N., Li, H., Liu, J., Liu, Z., Ma, L., Marland, G., Mayot, N., McGuire, P. C., McKinley, G. A., Meyer, G., Morgan, E. J., Munro, D. R., Nakaoka, S.-I., Niwa, Y., O'Brien, K. M., Olsen, A., Omar, A. M., Ono, T., Paulsen, M., Pierrot, D., Pocock, K., Poulter, B., Powis, C. M., Rehder, G., Resplandy, L., Robertson, E., Rödenbeck, C., Rosan, T. M., Schwinger, J., Séférian, R., Smallman, T. L., Smith, S. M., Sospedra-Alfonso, R., Sun, Q., Sutton, A. J., Sweeney, C., Takao, S., Tans, P. P., Tian, H., Tilbrook, B., Tsujino, H., Tubiello, F., van der Werf, G. R., van Ooijen, E., Wanninkhof, R., Watanabe, M., Wimart-Rousseau, C., Yang, D., Yang, X., Yuan, W., Yue, X., Zaehle, S., Zeng, J., and Zheng, B.: Global Carbon Budget 2023, Earth System Science Data, 15, 5301–5369, https://doi.org/10.5194/essd-15-5301-2023, 2023.

Gao, B.-C.: Normalized difference water index for remote sensing of vegetation liquid water from space, in: Imaging Spectrometry, vol. 2480 of Society of Photo-Optical Instrumentation Engineers (SPIE) Conference Series, edited by: Descour, M. R., Mooney, J. M., Perry, D. L., and Illing, L. R., 225–236, https://doi.org/10.1117/12.210877, 1995.

Gerbig, C.: Parameters for the Vegetation Photosynthesis and Respiration Model VPRM, ICOS, https://doi.org/10.18160/HF4C-G0KK, 2024.

Gerbig, C. and Koch, F.-T.: Biosphere-atmosphere exchange fluxes for CO_2 from the Vegetation Photosynthesis and Respiration Model VPRM for 2006–2021 (Version 1.0), ICOS, https://doi.org/10.18160/VX78-HVA1, 2021.

Gerbig, C. and Koch, F.-T.: Biosphere-atmosphere exchange fluxes for CO_2 from the Vegetation Photosynthesis and Respiration Model VPRM for 2022–2023, ICOS, https://doi.org/10.18160/R5HS-YKW0, 2024.

Glauch, T.: tglauch/pyVPRM: Stable release, v5.0, Zenodo [code], https://doi.org/10.5281/zenodo.14355806, 2024 (code also available at: https://github.com/tglauch/pyVPRM, last access: 28 July 2025).

Gourdji, S. M., Karion, A., Lopez-Coto, I., Ghosh, S., Mueller, K. L., Zhou, Y., Williams, C. A., Baker, I. T., Haynes, K. D., and Whetstone, J. R.: A Modified Vegetation Photosynthesis and Respiration Model (VPRM) for the Eastern USA and Canada, Evaluated With Comparison to Atmospheric Observations and Other Biospheric Models, J. Geophys. Res.-Biogeo., 127, e2021JG006290, https://doi.org/10.1029/2021JG006290, 2022.

Hardiman, B. S., Wang, J. A., Hutyra, L. R., Gately, C. K., Getson, J. M., and Friedl, M. A.: Accounting for urban biogenic fluxes in regional carbon budgets, Sci. Total Environ., 592, 366–372, https://doi.org/10.1016/j.scitotenv.2017.03.028, 2017.

Hersbach, H., Bell, B., Berrisford, P., Hirahara, S., Horányi, A., Muñoz-Sabater, J., Nicolas, J., Peubey, C., Radu, R., Schepers, D., Simmons, A., Soci, C., Abdalla, S., Abellan, X., Balsamo, G., Bechtold, P., Biavati, G., Bidlot, J., Bonavita, M., De Chiara, G., Dahlgren, P., Dee, D., Diamantakis, M., Dragani, R., Flemming, J., Forbes, R., Fuentes, M., Geer, A., Haimberger, L., Healy,

S., Hogan, R. J., Hólm, E., Janisková, M., Keeley, S., Laloyaux, P., Lopez, P., Lupu, C., Radnoti, G., de Rosnay, P., Rozum, I., Vamborg, F., Villaume, S., and Thépaut, J.-N.: The ERA5 global reanalysis, Q. J. Roy. Meteorol. Soc., 146, 1999–2049, https://doi.org/10.1002/qj.3803, 2020.

Hill, C., DeLuca, C., Balaji, Suarez, M., and Da Silva, A.: The architecture of the Earth System Modeling Framework, Comput. Sci. Eng., 6, 18–28, https://doi.org/10.1109/MCISE.2004.1255817, 2004.

Huete, A., Didan, K., Miura, T., Rodriguez, E., Gao, X., and Ferreira, L.: Overview of the radiometric and biophysical performance of the MODIS vegetation indices, Remote Sens. Environ., 83, 195–213, https://doi.org/10.1016/S0034-4257(02)00096-2, 2002.

ICOS RI, Aalto, J., Aiguier, T., Alivernini, A., Aluome, C., Andersson, T., Arriga, N., Aurela, M., Back, J., Barten, S., Baur, T., Bazot, S., Beauclair, P., Becker, N., Becker, N., Belelli Marchesini, L., Bergström, G., Bernhofer, C., Berveiller, D., Biermann, T., Bloor, J., Bodson, B., Bogaerts, G., Bortoli, M., Bosio, I., Brut, A., Brümmer, C., Buchmann, N., Buysse, P., Bâth, A., Calandrelli, D., Cavagna, M., Ceschia, E., Chabbi, A., Chebbi, W., Chianucci, F., Chipeaux, C., Chopin, H., Claverie, N., Cobbe, I., Colosse, D., Conte, A., Corsanici, R., Courtois, P., Coyle, M., Crill, P., Cuntz, M., Cuocolo, D., Czerný, R., DEPUYDT, J., Darenová, E., Darsonville, O., De Ligne, A., De Meulder, T., De Simon, G., Decau, M.-L., Dell'Acqua, A., Delorme, J.-P., Delpierre, N., Demoulin, L., Denou, J.-L., Di Matteo, B., Di Tommasi, P., Dienstbach, L., Dignam, R., Dolfus, D., Domec, J.-C., Douxfils, B., Dufrêne, E., Dumont, B., Durand, B., Eichelmann, U., Engelmann, T., Esposito, A., Esser, O., Etzold, S., Eugster, W., Famulari, D., Fares, S., Faurès, A., Feigenwinter, I., Feldmann, I., Fincham, W., Fischer, M., Foltýnová, L., Friborg, T., Galliot, J.-N., Garcia Quiros, I., Garrigou, C., Gasbarra, D., Gessler, A., Gharun, M., Gianelle, D., Gimper, S., Goded, I., Graf, A., Granouillac, F., Grenier, M., Grudd, H., Grünwald, T., Guillot, T., Harvey, D., Hatakka, J., Haustein, A., Hehn, M., Heinesch, B., Helfter, C., Heliasz, M., Holst, J., Holst, T., Hug, C., Häni, M., Hörtnagl, L., Ibrom, A., Ilardi, F., Jackowicz-Korczynski, M. A., Janssens, I., Jensen, R., Jocher, G., Joetzjer, E., Jones, M., Kempf, J., Kettler, M., Kljun, N., Klumpp, K., Kolari, P., Korrensalo, A., Kowalska, N., Kozii, N., Krejza, J., Kristoffersson, A., Kruijt, B., Kruszewski, A., Kumar, S., Kummer, S., Laakso, H., Lafont, S., Lange Rønn, E., Larmanou, E., Laurila, T., Leeson, S., Lefevre, L., Lehner, I., Lemaire, B., Levula, J., Levy, P., Liechti, K., Lily, J.-B., Limousin, J.-M., Linderson, M.-L., Lindgren, K., Lohila, A., Longdoz, B., Lootens, R., Loubet, B., Loustau, D., Lundin, E., López-Blanco, E., Löfvenius, P., Magliulo, V., Mammarella, I., Manco, A., Manise, T., Marcolla, B., Marek, M. V., Marklund, P., Marloie, O., Martin, R., Martin Saint Paul, N., Marty, M., Matilainen, T., Mattes, J., Matteucci, M., Mauder, M., Meier, P., Meire, A., Meis, J., Mensah, C., Michaud, L., Minerbi, S., Moderow, U., Montagnani, L., Moretti, V., Morfin, A., Mullinger, N., Mäkelä, T., Männikkö, M., Männistö, E., Mölder, M., Møller, F., Naiken, A., Naseer, M., Nemitz, E., Nezval, O., Nilsson, M., Orgun, A., Ottosson-Löfvenius, M., Ourcival, J.-M., Paasch, S., Pavelka, M., Peichl, M., Perot-Guillaume, C., Perrot, C., Pihlatie, M., Pilegaard, K., Piret, A., Prasse, H., Pumpanen, J., Rainne, J., Rakos, N., Rasmussen, L., Rebmann, C., Rinne, J., Rodeghiero, M., Roland, M.,

Rudd, D., Røjle Christensen, T., Schaarup Sørensen, J., Schmidt, M., Schmidt, P., Schmitt Oehler, M., Schrader, F., Segers, J., Simioni, G., Smith, P., Snellen, H., Sorgi, T., Soudani, K., Staník, K., Staudinger, M., Stecher, M., Stutz, T., Suopajärvi, S., Sutter, F., Taipale, R., Tallec, T., Tenca, F., Thimonier Rickenmann, A., Thyrion, T., Tomelleri, E., Tosca, M., Trotsiuk, V., Trusina, J., Tuittila, E.-S., Tuovinen, J.-P., Tyssandier, J., Tülp, H., Van Look, J., Varjonen, S., Vesala, T., Vescovo, L., Vincent, G., Vincke, C., Vitale, L., Vágner, L., Waldner, P., Wiesen, R., Winck, B., Yeung, K., Zampedri, R., Zawilski, B., Zenone, T., Zimmermann, S., Zweifel, R., van Dijk, N., van der Molen, M., Öquist, M., Šigut, L., Šlížek, J., and ICOS ETC: Ecosystem final quality (L2) product in ETC-Archive format – INTERIM release 2023–2, ICOS [data set], https://doi.org/10.18160/JYAR-7YEH, 2023.

Järvi, L., Nordbo, A., Junninen, H., Riikonen, A., Moilanen, J., Nikinmaa, E., and Vesala, T.: Seasonal and annual variation of carbon dioxide surface fluxes in Helsinki, Finland, in 2006–2010, Atmos. Chem. Phys., 12, 8475–8489, https://doi.org/10.5194/acp-12-8475-2012, 2012.

Jiang, Z., Huete, A. R., Didan, K., and Miura, T.: Development of a two-band enhanced vegetation index without a blue band, Remote Sens. Environ., 112, 3833–3845, https://doi.org/10.1016/j.rse.2008.06.006, 2008.

Jung, M., Henkel, K., Herold, M., and Churkina, G.: Exploiting synergies of global land cover products for carbon cycle modeling, Remote Sens. Environ., 101, 534–553, https://doi.org/10.1016/j.rse.2006.01.020, 2006.

Luus, K. A. and Lin, J. C.: The Polar Vegetation Photosynthesis and Respiration Model: a parsimonious, satellite-data-driven model of high-latitude CO_2 exchange, Geosci. Model Dev., 8, 2655–2674, https://doi.org/10.5194/gmd-8-2655-2015, 2015.

Mahadevan, P., Wofsy, S. C., Matross, D. M., Xiao, X., Dunn, A. L., Lin, J. C., Gerbig, C., Munger, J. W., Chow, V. Y., and Gottlieb, E. W.: A satellite-based biosphere parameterization for net ecosystem CO_2 exchange: Vegetation Photosynthesis and Respiration Model (VPRM), Global Biogeochem. Cy., 22, GB2005, https://doi.org/10.1029/2006GB002735, 2008.

Maksyutov, S., Eggleston, S., Woo, J. H., Fang, S., Witi, J., Gillenwater, M., Goodwin, J., and Tubiello, F.: Quality Assurance/Quality Control and Verification, 2019 Refinement to the 2006 IPCC Guidelines for National Greenhouse Gas Inventories, IPCC, https://www.ipcc-nggip.iges.or.jp/public/2019rf/pdf/1_Volume1/19R_V1_Ch06_QA_QC.pdf (last access: 14 September 2024), 2019.

Matross, D. M., Arlyn Andrews, M. P., Gerbig, C., Lin, J. C., Wofsy, S. C., Daube, B. C., Gottlieb, E. W., Chow, V. Y., John T. Lee, C. Z., Bakwin, P. S., Munger, J. W., and Hollinger, D. Y.: Estimating regional carbon exchange in New England and Quebec by combining atmospheric, ground-based and satellite data, Tellus B, 58, 344–358, https://doi.org/10.1111/j.1600-0889.2006.00206.x, 2006.

Monteil, G., Broquet, G., Scholze, M., Lang, M., Karstens, U., Gerbig, C., Koch, F.-T., Smith, N. E., Thompson, R. L., Luijkx, I. T., White, E., Meesters, A., Ciais, P., Ganesan, A. L., Manning, A., Mischurow, M., Peters, W., Peylin, P., Tarniewicz, J., Rigby, M., Rödenbeck, C., Vermeulen, A., and Walton, E. M.: The regional European atmospheric transport inversion comparison, EUROCOM: first results on European-wide terrestrial carbon fluxes for the period 2006–2015, Atmos. Chem. Phys., 20, 12063–12091, https://doi.org/10.5194/acp-20-12063-2020, 2020.

Moreno-Martínez, A., Izquierdo-Verdiguier, E., Maneta, M. P., Camps-Valls, G., Robinson, N., Muñoz-Marí, J., Sedano, F., Clinton, N., and Running, S. W.: Multispectral high resolution sensor fusion for smoothing and gap-filling in the cloud, Remote Sensi. Environ., 247, 111901, https://doi.org/10.1016/j.rse.2020.111901, 2020.

Munassar, S., Rödenbeck, C., Koch, F.-T., Totsche, K. U., Gałkowski, M., Walther, S., and Gerbig, C.: Net ecosystem exchange (NEE) estimates 2006–2019 over Europe from a pre-operational ensemble-inversion system, Atmos. Chem. Phys., 22, 7875–7892, https://doi.org/10.5194/acp-22-7875-2022, 2022.

Muñoz Sabater, J., Dutra, E., Agustí-Panareda, A., Albergel, C., Arduini, G., Balsamo, G., Boussetta, S., Choulga, M., Harrigan, S., Hersbach, H., Martens, B., Miralles, D. G., Piles, M., Rodríguez-Fernández, N. J., Zsoter, E., Buontempo, C., and Thépaut, J.-N.: ERA5-Land: a state-of-the-art global reanalysis dataset for land applications, Earth Syst. Sci. Data, 13, 4349–4383, https://doi.org/10.5194/essd-13-4349-2021, 2021.

Nelson, J. A., Walther, S., Gans, F., Kraft, B., Weber, U., Novick, K., Buchmann, N., Migliavacca, M., Wohlfahrt, G., Šigut, L., Ibrom, A., Papale, D., Göckede, M., Duveiller, G., Knohl, A., Hörtnagl, L., Scott, R. L., Zhang, W., Hamdi, Z. M., Reichstein, M., Aranda-Barranco, S., Ardö, J., Op de Beeck, M., Billdesbach, D., Bowling, D., Bracho, R., Brümmer, C., Camps-Valls, G., Chen, S., Cleverly, J. R., Desai, A., Dong, G., El-Madany, T. S., Euskirchen, E. S., Feigenwinter, I., Galvagno, M., Gerosa, G., Gielen, B., Goded, I., Goslee, S., Gough, C. M., Heinesch, B., Ichii, K., Jackowicz-Korczynski, M. A., Klosterhalfen, A., Knox, S., Kobayashi, H., Kohonen, K.-M., Korkiakoski, M., Mammarella, I., Mana, G., Marzuoli, R., Matamala, R., Metzger, S., Montagnani, L., Nicolini, G., O'Halloran, T., Ourcival, J.-M., Peichl, M., Pendall, E., Ruiz Reverter, B., Roland, M., Sabbatini, S., Sachs, T., Schmidt, M., Schwalm, C. R., Shekhar, A., Silberstein, R., Silveira, M. L., Spano, D., Tagesson, T., Tramontana, G., Trotta, C., Turco, F., Vesala, T., Vincke, C., Vitale, D., Vivoni, E. R., Wang, Y., Woodgate, W., Yepez, E. A., Zhang, J., Zona, D., and Jung, M.: X-BASE: the first terrestrial carbon and water flux products from an extended data-driven scaling framework, FLUXCOM-X, EGUsphere [preprint], https://doi.org/10.5194/egusphere-2024-165, 2024.

Niu, S., Chen, W., Liáng, L. L., Sierra, C. A., Xia, J., Wang, S., Heskel, M., Patel, K. F., Bond-Lamberty, B., Wang, J., Yvon-Durocher, G., Kirschbaum, M. U. F., Atkin, O. K., Huang, Y., Yu, G., and Luo, Y.: Temperature responses of ecosystem respiration, Nat. Rev. Earth Environ., 5, 559–571, https://doi.org/10.1038/s43017-024-00569-3, 2024.

Pastorello, G., Trotta, C., Canfora, E., Chu, H., Christianson, D., Cheah, Y.-W., Poindexter, C., Chen, J., Elbashandy, A., Humphrey, M., Isaac, P., Polidori, D., Ribeca, A., van Ingen, C., Zhang, L., Amiro, B., and Ammann, C.: The FLUXNET2015 dataset and the ONEFlux processing pipeline for eddy covariance data, Sci. Data, 7, 225, https://doi.org/10.1038/s41597-020-0534-3, 2020.

Paulus, S. J., Orth, R., Lee, S.-C., Hildebrandt, A., Jung, M., Nelson, J. A., El-Madany, T. S., Carrara, A., Moreno, G., Mauder, M., Groh, J., Graf, A., Reichstein, M., and Migliavacca, M.: Interpretability of negative latent heat fluxes from eddy covariance measurements in dry conditions, Biogeosciences, 21, 2051–2085, https://doi.org/10.5194/bg-21-2051-2024, 2024.

Peckham, S. E.: WRF/Chem version 3.3 user's guide, NOAA, https://repository.library.noaa.gov/view/noaa/11119 (last access: 25 July 2025), 2012.

Randerson, J. T., Thompson, M. V., Malmstrom, C. M., Field, C. B., and Fung, I. Y.: Substrate limitations for heterotrophs: Implications for models that estimate the seasonal cycle of atmospheric CO_2, Global Biogeochem. Cy., 10, 585–602, 1996.

Reichstein, M., Falge, E., Baldocchi, D., Papale, D., Aubinet, M., Berbigier, P., Bernhofer, C., Buchmann, N., Gilmanov, T., Granier, A., Grünwald, T., Havránková, K., Ilvesniemi, H., Janous, D., Knohl, A., Laurila, T., Lohila, A., Loustau, D., Matteucci, G., Meyers, T., Miglietta, F., Ourcival, J.-M., Pumpanen, J., Rambal, S., Rotenberg, E., Sanz, M., Tenhunen, J., Seufert, G., Vaccari, F., Vesala, T., Yakir, D., and Valentini, R.: On the separation of net ecosystem exchange into assimilation and ecosystem respiration: review and improved algorithm, Global Change Biol., 11, 1424–1439, https://doi.org/10.1111/j.1365-2486.2005.001002.x, 2005.

Roberts, C. D., Senan, R., Molteni, F., Boussetta, S., Mayer, M., and Keeley, S. P. E.: Climate model configurations of the ECMWF Integrated Forecasting System (ECMWF-IFS cycle 43r1) for HighResMIP, Geosci. Model Dev., 11, 3681–3712, https://doi.org/10.5194/gmd-11-3681-2018, 2018.

Rouse, J. W., Haas, R. H., Schell, J. A., and Deering, D. W.: Monitoring vegetation systems in the Great Plains with ERTS, NASA Spec. Publ. 351, NASA, 309 pp., https://ntrs.nasa.gov/citations/19740022614 (last access: 24 July 2025), 1974.

Running, S. and Zhao, M.: MODIS/Terra net primary production gap-filled yearly L4 global 500 m SIN grid V061, NASA, https://doi.org/10.5067/MODIS/MOD17A3H.006, 2021.

Sargent, M., Barrera, Y., Nehrkorn, T., Hutyra, L. R., Gately, C. K., Jones, T., McKain, K., Sweeney, C., Hegarty, J., Hardiman, B., Wang, J. A., and Wofsy, S. C.: Anthropogenic and biogenic CO_2 fluxes in the Boston urban region, P. Natl. Acad. Sci. USA, 115, 7491–7496, https://doi.org/10.1073/pnas.1803715115, 2018.

Schmid, H.: Source areas for scalars and scalar fluxes, Bound.-Lay. Meteorol., 67, 293–318, 1994.

Scholze, M., Kaminski, T., Knorr, W., Voßbeck, M., Wu, M., Ferrazzoli, P., Kerr, Y., Mialon, A., Richaume, P., Rodríguez-Fernández, N., Vittucci, C., Wigneron, J.-P., Mecklenburg, S., and Drusch, M.: Mean European Carbon Sink Over 2010–2015 Estimated by Simultaneous Assimilation of Atmospheric CO_2, Soil Moisture, and Vegetation Optical Depth, Geophys. Res. Lett., 46, 13796–13803, https://doi.org/10.1029/2019GL085725, 2019.

Schröter, J., Rieger, D., Stassen, C., Vogel, H., Weimer, M., Werchner, S., Förstner, J., Prill, F., Reinert, D., Zängl, G., Giorgetta, M., Ruhnke, R., Vogel, B., and Braesicke, P.: ICON-ART 2.1: a flexible tracer framework and its application for composition studies in numerical weather forecasting and climate simulations, Geosci. Model Dev., 11, 4043–4068, https://doi.org/10.5194/gmd-11-4043-2018, 2018.

Souza, C. M., Z. Shimbo, J., Rosa, M. R., Parente, L. L., A. Alencar, A., Rudorff, B. F. T., Hasenack, H., Matsumoto, M., G. Ferreira, L., Souza-Filho, P. W. M., de Oliveira, S. W., Rocha, W. F., Fonseca, A. V., Marques, C. B., Diniz, C. G., Costa, D., Monteiro, D., Rosa, E. R., Vélez-Martin, E., Weber, E. J., Lenti, F. E. B., Paternost, F. F., Pareyn, F. G. C., Siqueira, J. V., Viera, J. L., Neto, L. C. F., Saraiva, M. M., Sales, M. H., Salgado, M. P. G., Vasconcelos, R., Galano, S., Mesquita, V. V., and Azevedo, T.: Reconstructing Three Decades of Land Use and Land Cover Changes in Brazilian Biomes with Landsat Archive and Earth Engine, Remote Sensing, 12, 2735, https://doi.org/10.3390/rs12172735, 2020.

Stocker, B. D., Zscheischler, J., Keenan, T. F., Prentice, I. C., Seneviratne, S. I., and Peñuelas, J.: Drought impacts on terrestrial primary production underestimated by satellite monitoring, Nat. Geosci., 12, 264–270, https://doi.org/10.1038/s41561-019-0318-6, 2019.

Sun, W., Luo, X., Fang, Y., Shiga, Y. P., Zhang, Y., Fisher, J. B., Keenan, T. F., and Michalak, A. M.: Biome-scale temperature sensitivity of ecosystem respiration revealed by atmospheric CO_2 observations, Nat. Ecol. Evol., 7, 1199–1210, https://doi.org/10.1038/s41559-023-02093-x, 2023.

Swinbank, W. C.: The Measurement of Vertical Transfer of Heat and Water Vapor by Eddies in the Lower Atmosphere, J. Atmos. Sci., 8, 135–145, https://doi.org/10.1175/1520-0469(1951)008<0135:TMOVTO>2.0.CO;2, 1951.

Thompson, R. L., Broquet, G., Gerbig, C., Koch, T., Lang, M., Monteil, G., Munassar, S., Nickless, A., Scholze, M., Ramonet, M., Karstens, U., van Schaik, E., Wu, Z., and Rödenbeck, C.: Changes in net ecosystem exchange over Europe during the 2018 drought based on atmospheric observations, Philos. T. Roy. Soc. B, 375, 20190512, https://doi.org/10.1098/rstb.2019.0512, 2020.

Vermote, E.: MODIS/Terra Surface Reflectance 8-Day L3 Global 500 m SIN Grid V061, USGS [data set], https://doi.org/10.5067/MODIS/MOD09A1.061, 2021a.

Vermote, E.: MODIS/Aqua Surface Reflectance 8-Day L3 Global 500 m SIN Grid V061, USGS, https://doi.org/10.5067/MODIS/MYD09A1.061, 2021b.

Vermote, E. and Wolfe, R.: MODIS/Terra Surface Reflectance Daily L2G Global 1 km and 500 m SIN Grid V061, USGS [data set], https://doi.org/10.5067/MODIS/MOD09GA.061, 2021.

Vermote, E., Franch, B., and Claverie, M.: VIIRS/NPP Surface Reflectance Daily L2G Global 1 km and 500 m SIN Grid V002, USGS [data set], https://doi.org/10.5067/VIIRS/VNP09GA.002, 2023a.

Vermote, E., Franch, B., and Claverie, M.: VIIRS/NPP Surface Reflectance 8-Day L3 Global 500 m SIN Grid V002, USGS [data set], https://doi.org/10.5067/VIIRS/VNP09H1.002, 2023b.

Wutzler, T., Lucas-Moffat, A., Migliavacca, M., Knauer, J., Sickel, K., Šigut, L., Menzer, O., and Reichstein, M.: Basic and extensible post-processing of eddy covariance flux data with REddyProc, Biogeosciences, 15, 5015–5030, https://doi.org/10.5194/bg-15-5015-2018, 2018.

Zanaga, D., Van De Kerchove, R., Daems, D., De Keersmaecker, W., Brockmann, C., Kirches, G., Wevers, J., Cartus, O., Santoro, M., Fritz, S., Lesiv, M., Herold, M., Tsendbazar, N.-E., Xu, P., Ramoino, F., and Arino, O.: ESA WorldCover 10 m 2021 v200, Zenodo [data set], https://doi.org/10.5281/zenodo.7254221, 2022.

Zhuang, J., raphael dussin, Huard, D., Bourgault, P., Banihirwe, A., Raynaud, S., Malevich, B., Schupfner, M., Filipe, Levang, S., Gauthier, C., Jüling, A., Almansi, M., RichardScottOZ, RondeauG, Rasp, S., Smith, T. J., Stachelek, J., Plough, M., Pierre, Bell, R., Caneill, R., and Li, X.: pangeo-data/xESMF: v0.8.2, Zenodo [data set], https://doi.org/10.5281/zenodo.8356796, 2023.